Massive pre-stellar cores in radiation-magneto-turbulent simulations of molecular clouds

Chong-Chong He ⓘ★ and Massimo Ricotti ⓘ★

Department of Astronomy, University of Maryland, College Park, MD 20742, USA

ABSTRACT

We simulate the formation and collapse of pre-stellar cores at few-au resolution in a set of radiation-magnetohydrodynamic simulations of giant molecular clouds (GMCs) using the grid-based code RAMSES-RT. We adopt, for the first time to our best knowledge, realistic initial/boundary conditions by zooming in on to individual massive pre-stellar cores within the GMC. We identify two distinct modes of fragmentation: 'quasi-spherical' and 'filamentary'. In both modes, the fragments eventually become embedded in a quasi-steady accretion disc or toroid with radii $\sim$500–5000 au and opening angles $H/R \sim 0.5 - 1$. The discs/toroids are Toomre stable but the accreted pre-existing fragments are found orbiting the outer disc, appearing as disc fragmentation. Each core converts nearly 100 per cent of the gas mass into a few massive stars forming near the disc centre. Large and massive discs around high-mass stars are supported by magnetic pressure in the outer disc, at radii $>$200–1000 au, and turbulent pressure in the inner disc. The most massive core accretes several times more mass than its initial mass, forming a cluster of 8 massive (proto)stars enshrouded by a toroid, suggesting a competitive accretion scenario for the formation of stars above $\sim$30 $M_\odot$. We also find that the H II regions produced by a single massive star remain trapped in the dense circumstellar discs for a few hundred kiloyears, while the dynamic motions of massive stars in wide binaries or multiple systems displace the stars from the densest parts of the disc, allowing UV radiation to escape producing steady or pulsating bipolar H II regions.

Key words: MHD – stars: formation – stars: massive – stars: protostars.

1 INTRODUCTION

Whether high-mass (HM) stars form from the monolithic collapse of massive pre-stellar cores – supported by turbulence, and/or magnetic fields rather than thermal pressure – known as the turbulent core (TC) scenario (McKee & Tan 2003; Tan et al. 2014), or via accretion inflows from larger scales, known as the competitive accretion (CA) scenario (Bonnell et al. 2001; Padoan et al. 2020), still remains an open question. Observations (Fuller, Williams & Sridharan 2005; van der Tak et al. 2019) of accreting HM young stellar objects (YSOs) suggest that HM stars form similar to their low-mass counterparts via infall from a surrounding envelope and from anisotropic accretion flow from an accretion disc. However, the physical processes involved are not well understood partially due to the lack of high-resolution observations of structures below $\sim$1000 au owing to the large distances of the sources, high dust extinction, high multiplicity, and complexity of the environment typical of HM star formation. The shorter time-scale of formation and rarity of the objects result in a low probability of finding a O-type massive (proto)star or massive starless core.

The CA model postulates that low-mass protostellar seeds accrete unbound gas within the clump from large scales in a hierarchical structure. To test the idea of the CA scenario from a theoretical perspective, we need to simulate the formation of pre-stellar cores from the collapse of turbulent giant molecular clouds (GMCs),

which is the site of star formation. Several numerical studies have investigated the formation of star clusters from GMCs (Jones & Bate 2018; Kim, Kim & Ostriker 2018; Lee & Hennebelle 2018; Bate 2019; Fukushima et al. 2020; Grudić et al. 2021; Kim, Ostriker & Filippova 2021). In He, Ricotti & Geen (2019, 2020), we have conducted a series of simulations of the collapse of isolated turbulent GMCs using RAMSES-RT. In these works we have run a large grid of GMC simulations and pushed the parameters of the GMC mass and density to include very massive ($\sim$10^5 $M_\odot$) and extremely dense ($\sim$10^4 cm^{-3}) clouds, resolving the formation of individual stars with masses $M \gtrsim 1$ $M_\odot$, significantly improving the resolution with respect to previous works (see a summary in table 2 of Lee & Hennebelle 2018). The initial mass functions (IMFs) of the stars forming in these simulations have not only characteristic power-law slopes very close to Kroupa (2002) at the HM end, but also the correct normalization to a mass-normalized Kroupa IMF if we assume that each sink particle converts ~ 40 per cent of its mass to a single star and the remaining mass forms several smaller mass stars. This scaling is also inferred from the mapping between the observed core mass function (CMF) and stellar IMF that preserves the slope and normalization of the IMF. Hence, we hypothesize that the unresolved sinks in the simulation form stars with high efficiency but fragment into lower mass stars.

Motivated by these previous results, in this work we aim at testing our assumption on the fragmentation of sink particles in order to understand the mass function, star multiplicity, and kinematics which is important to eventually understand the long-term evolution of the star cluster and a possible role of high-z compact star clusters

★ E-mail: che1234@umd.edu (CCH); ricotti@umd.edu (MR)

in forming and growing intermediate-mass black holes (IMBHs) seeds. The methodology we use is to perform higher resolution 'zoom' simulations of the fragmenting protostellar cores, while simultaneously following the collapse of the GMC in which the cores are located.

There is growing evidence from ALMA observations that accretion discs around massive proto-stars undergo fragmentation and produce companion stars (e.g. Johnston et al. 2015; Guzmán et al. 2020; Olguin et al. 2022; Williams et al. 2022). Ilee et al. (2018) reported the observation of a fragmented Keplerian disc around an O-type protostar, with a fragment in the outskirts of the disc at ~2000 au from the primary. Johnston et al. (2020) observed spiral arms and instability in a disc of radius ~1000 au around an O-type star.

Discs are observed to not only possess substructures in the (r, θ) plane, but also show clear signs of substructures in the vertical (z) direction (Muzerolle et al. 2009; Espaillat et al. 2011). Warped geometries or misalignment ('broken' discs) have been inferred kinematically with resolved spectral line data (Rosenfeld et al. 2012; Casassus et al. 2015) and scatter light shadows at larger r (Marino, Perez & Casassus 2015).

A considerable amount of research has studied discs around nearby solar-type stars. However, the number of disc studied around more distant, massive stars (type A and earlier) is comparatively small. This is because massive protostellar cores that may form massive stars, multiple systems or even a mini-cluster of stars are fewer and short-lived, and hence are less likely to be found nearby.

Recent advances in radio/mm and optical/IR interferometers have enabled important progress in the field of discs around intermediate-mass (IM) and HM YSOs. These observations of embedded IM protostars (A to late-B spectral type; Zapata et al. 2007; Sánchez-Monge et al. 2010; Takahashi et al. 2012; van Kempen et al. 2012) have revealed circumstellar discs with typical radii of a few hundred of au. These discs are geometrically thick with a scale height that is more than 20–30 per cent of their radius. The discs have masses of a few solar masses and could be in Keplerian rotation. Evidence for circumstellar discs has been reported (Cesaroni et al. 2005; Patel et al. 2005; Kraus et al. 2010; de Wit et al. 2011; Ginsburg et al. 2018; Law et al. 2022) for HM (proto)stars (early-B to late-O type) that correspond to zero-age main-sequence stars of about 25–30 $M_\odot$ with typical radii of a few thousands of au, although radii smaller than 1000 au have been estimated in some samples. These geometrically thick structures have scale heights of >30–40 per cent of their radii and masses that range from a few $M_\odot$ to a few tens of $M_\odot$. They are gravitationally stable as suggested by Toomre's stability parameter $Q > 1$. In short, the basic properties of the discs around HM (proto)stars appear as a scaled-up version of those found for discs around low-mass and intermediate-mass protostars (see Beltrán & de Wit 2016, for a review).

For stars of extremely high mass ($>30\,M_\odot$), the existence of a circumstellar disc has been elusive in observations. Simulations have shown that radiation pressure does not prevent disc accretion to form stars up to 140 $M_\odot$ (Krumholz et al. 2009; Kuiper et al. 2010). However, no models of protostars allow the formation of a hydrostatic object beyond this limit. Large, dense ($n \gtrsim 10^7\,\mathrm{cm}^{-3}$) and massive (a few $\times$ 100 $M_\odot$) rotating cores have been detected around early-O-type protostars. These are likely non-equilibrium structures that favour the formation of young stellar mini-clusters instead of individual massive stars (Cesaroni et al. 2007; Beltrán et al. 2011).

In this work, we study the collapse of pre-stellar cores and the structure of protostellar discs around massive stars in realistic simulations of turbulent GMCs. These discs span a large range in sizes and masses. In this paper, we emphasize the dominant role

of turbulence and magnetic field in determining the formation and support against the gravity of massive discs within pre-stellar cores. In a companion paper, we will address in more detail the structure and evolution of the magnetic field and the problem of magnetic braking.

The rest of this article is organized as follows. We describe our simulation method in Section 2. We present the basic results in Section 3, where we discuss the formation of turbulent massive discs. In Section 4, we discuss the properties of the core fragments. We provide discussions and the summary in Section 5.

2 METHODS AND SIMULATIONS

We conduct 'zoom-in' radiation-MHD simulations of collapsing molecular clouds resolving individual pre-stellar cores. We focus on the fragmentation of the cores and the formation of protostellar discs. We have conducted a set of 6 simulations on a large range of sink masses selected from several parental GMCs. We summarize the key parameters and results in Table 1.

We perform simulations using the grid-based adaptive mesh refinement (AMR) MHD code RAMSES-RT (Teyssier 2002; Fromang, Hennebelle & Teyssier 2006). Radiation transfer is modelled using a moment-based method with the M1 closure relation for the Eddington tensor (Rosdahl et al. 2013). The ionizing photons emitted from stars interact with neutral gas and we keep track of the ionization chemistry of hydrogen and helium, but we do not include the chemical evolution of the molecular phase. Heating from photoionization and cooling from hydrogen, helium, metals, and dust grains are implemented (see Geen, Soler & Hennebelle 2017 for details). Cooling below 10 K is shut down to keep the temperature floor at 10 K. We carry out simulations starting from a subset of simulations presented in He et al. (2019) and zooming into pre-stellar cores to resolve their fragmentation and disc formation. We refer to the original paper for details of the method and key results of these baseline simulations. Here, we briefly summarize the AMR technique and sink particle recipe before getting into the zoom-in method.

The baseline simulations (He et al. 2019) are started from idealized spherical isothermal clouds in hydrostatic equilibrium surrounded by a low-density shell, in which gravity is nearly balanced by turbulent motions ($\alpha_{\mathrm{vir}} \equiv \mathcal{K}/|\mathcal{W}| = 0.4$). We let the GMC evolve for three free-fall times with gravity reduced by 1/2, to allow the turbulence to develop. Then, gravity is fully turned on and the cloud undergoes filamentary collapse and fragments to form sink particles in dense regions that represent singular stars or small clusters of stars, as described in Bleuler & Teyssier (2014). Adaptive mesh refinement is applied to the whole domain to make sure at any time and any location the local Jeans length, $L_J = c_s \sqrt{\pi/(G\rho)}$, is resolved by at least 10 grid points. The maximum refinement level $l_{\max}$ is set to 14, reaching a minimum grid size $\Delta x_{\min}$ that is $1/2^{14}$ of the box size, or around 200–1600 au. When the density reaches the critical density, n_{sink}, defined such that the corresponding Jeans length equals $5\times$ the grid size at the maximum refinement level $l_{\max}$, a sink particle is placed to prevent the increase of the gas density beyond n_{sink} at which a local Jeans length is not fully resolved. The critical density for sink formation is set to $n_{\mathrm{sink}} = 2.16 \times 10^{10}\,\mathrm{cm}^{-3}(\Delta x_{\min}/10\,\mathrm{au})^{-2}$, motivated by the criterion that a Jeans length must be resolved by no less than 5 grids. The corresponding Jeans mass is 0.0055 $M_\odot(\Delta x_{\min}/10\,\mathrm{au})$. In the baseline simulations in He et al. (2019) used as initial conditions, n_{sink} ranges from 10^6 to $6 \times 10^7\,\mathrm{cm}^{-3}$, while in the zoom-in simulations presented here, we reach densities three orders of magnitude higher: n_{sink} ranges from 10^9 to $5 \times 10^{10}\,\mathrm{cm}^{-3}$. Accretion on to the sink

Table 1. Summary of the properties of the simulated cores, protostellar discs, and forming stars. The discs with * are the primary focus of this article and are discussed extensively. Two other simulations, Core E and F, whose parameters lie within the parameter space of the cores listed here, are eliminated from this table for simplicity. The columns are, from left to right, (1) core names; (2) the mass of the gas/core above a threshold density 3000 cm⁻³, M_{core}; (3) the mass of the sink particle that forms in the lower resolution ($l_{max} = 14$) baseline run; (4) sink particle density; (5) the virial ratio $\alpha_{vir} = \mathcal{K}/|\mathcal{W}|$; (6) the ratio of the rotational energy to the gravitational energy of the initial core; (7) the mass-to-flux ratio; (8) the maximum resolution is $1/2^{l_{max}}$ of the box size; (9) sink particle density in the zoom-in simulations; (10) the maximum resolution (minimum cell size); (11) the total stellar mass in the 'zoom-in' run; (12) the maximum mass of the stars that form in the core; (13) the number of stars that form in the 'zoom-in' run; (14) the mode of core collapse (Fig. 3); (15) disc radius; (16) disc thickness; (17) disc aspect ratio.

Core	M_{core} (M$_\odot$)	$M_{\star,base}$ (M$_\odot$)	$n_{sink,base}$ (cm⁻³)	α_{vir}	β_{rot}	μ	l_{max}	Δx_{min} (au)	n_{sink} (cm⁻³)	$M_{\star,tot}$ (M$_\odot$)	$M_{\star,max}$ (M$_\odot$)	N_{stars}	Mode	R_{disc} (au)	H_{disc} (au)	H_{disc}/R_{disc}
A-hr*	27.7	12.0	1.4×10^7	0.270	0.095	3.146	20	7.2	5.7×10^{10}	12.6	4.9	12	Spherical	600	100–200	0.17–0.33
B*	119	309	3.0×10^6	0.489	0.071	2.351	18	60	7.7×10^8	>601	75.1	9	Filamentary	6000	3000	0.5–1.3
C	50.8	32.6	1.4×10^7	0.348	0.058	2.114	18	29	3.6×10^9	43.1	42.7	4	Spherical	200	100	0.5
D	63.3	8.4	6.5×10^6	0.182	0.060	1.826	18	42	1.7×10^9	14.7	14.7	1	Filamentary	600	200	0.33

particles is modelled using a threshold method such that 75 per cent of the mass above n_{sink} is transferred to the sink particle in each time-step (Bleuler & Teyssier 2014). Ionizing photos are emitted from the sink particles to ionize and heat the gas, dispersing the cloud, and quenching star formation. These sink particles in the baseline simulations are shown to resemble pre-stellar cores observed in local star-forming regions.

In the 'zoom-in' simulations presented in this paper, we start a simulation from a snapshot of a baseline AMR simulation right before the formation of a sink particle (Fig. 1). We define a 'zoom' region, about 0.5–1 pc in size, where the sink particle is about to form and allow a higher l_{max} only within this region. To reach the best possible resolution, we use a nested refinement structure where l_{max} increases as it gets closer to the domain centre. In the simulation with the best resolution (Core *A-hr*, as we will introduce later), l_{max} at the centre of the 'zoom-in' region is set to 20, reaching a dynamic range of $2^{20} \approx 10^6$, or 18 orders of magnitude in volume. The corresponding critical density of sink formation ρ_{sink} is 1.4×10^{-13} g cm⁻³, approaching the density at which the core transitions from isothermal to adiabatic (Masunaga, Miyama & Inutsuka 1998; Masunaga & Inutsuka 2000). The corresponding spatial resolution and other parameters for all simulations are listed in Table 1. This 'zoom-in' AMR method has been applied to MHD simulations of low-mass star formation without radiation feedback (Kuffmeier, Haugbølle & Nordlund 2017; Kuffmeier, Calcutt & Kristensen 2019). In this work, we report the first application of this method in radiation-MHD simulations of star formation.

Hydrogen and helium-ionizing photons are emitted from sinks and heat the gas. The hydrogen-ionizing luminosity of a sink particle with mass M_{sink} is given by

$$S = 9.63 \times 10^{48} \text{ s}^{-1} \left(\frac{0.4\ M_{sink}}{27.28\ \text{M}_\odot} \right)^{1.86}. \quad (1)$$

This is the same as the fits given in Vacca, Garmany & Shull (1996) for HM stars ($\gtrsim 30\,\text{M}_\odot$). However, Vacca et al. (1996) fits are described by a broken power law and have a steeper slope for masses $<10\,\text{M}_\odot$. Hence, we are overestimating the ionizing radiation emitted by stars with masses smaller than $\sim 10\,\text{M}_\odot$. The excess of ionizing photons from low/intermediate-mass stars is used to compensate for the lack of protostellar outflows or jets in our simulations. This recipe proved to be effective in reproducing the canonical IMF in our previous simulations (He et al. 2019).[1] However, we acknowledge that the lack of protostellar outflows and radiative heating (e.g. Krumholz, Klein & McKee 2007) in our feedback recipe may cause the gas temperature during the protostellar phase to be underestimated and the efficiency of conversion of core gas mass into stars to be overestimated. We also neglect radiation pressure from stars that could be important in HM star formation (e.g. Krumholz & Matzner 2009; Kuiper et al. 2010; Rosen et al. 2016). Further simulations with more realistic feedback mechanisms are left for future work.

We set a magnetic field with moderate strength in the *x*-direction threading the isothermal cloud in the initial conditions. The GMC starts from an idealized sphere with an isothermal core surrounded by a low-density shell that extends twice the radius. The magnetic

---

[1]In He et al. (2019), we adopted a broken power-law as in Vacca et al. (1996), but due to a bug in the code, the change in power-law slope at the low-mass end did happen at much lower masses. When we found and fixed the bug, we observed that the IMF at the HM end was not reproduced as well as before. We interpreted this result as the need for stronger feedback from the low-mass end, perhaps produced by protostellar outflows.
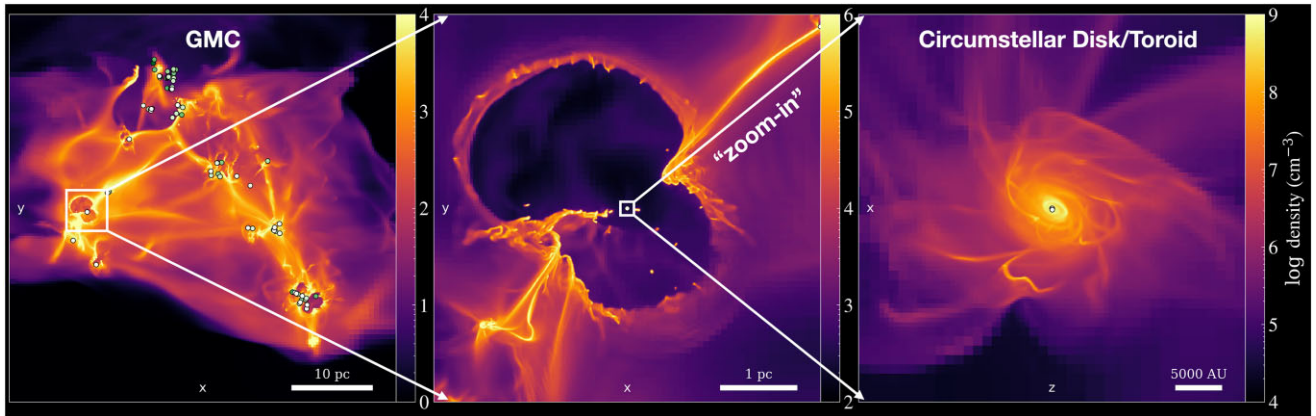
Figure 1. Outline of the simulation method. We pick a zoom region which is a box at the formation location of a sink particle. Inside the box, we allow a high level of refinement to reach high density before star formation. The whole simulation spans a dynamic range up to $2^{20} \approx 10^6$ in linear scale, or a volumetric dynamic range of 18 orders of magnitude.

intensity is about 10–25 μG at a density of 10^3 cm^{-3} and the mass-to-flux ratio is $\mu \approx 5$ averaged over the whole GMC. The value of μ in the isothermal core of the GMC is higher (≈ 8) due to the fact that the mass is more concentrated in the core but the magnetic field is more evenly distributed. After a period of relaxation to let the turbulence develop, the initial mean density decreases slightly and μ settles at 3–4, averaged over the whole molecular cloud. Instead of the traditional definition of the mass-to-flux ratio, $\mu \equiv M/M_\Phi$, where M_Φ is the magnetic critical mass, we adopt a definition that takes into account the non-homogeneity of the density and magnetic field, $\mu = \sqrt{|\mathcal{W}|/\mathcal{B}}$, where $\mathcal{W}$ is the gravitational binding energy and $\mathcal{B}$ is the magnetic energy. The two definitions are equivalent for a uniform spherical cloud with uniform magnetic field. We will explain further the derivation and significance of the μ parameter in Section 3.

The motion of the sink particles is determined by combining direct N-body integration (using the leapfrog method) between the sinks and between the sinks and the gas based on the particle mesh method. A softening length of $2\Delta x_{\min}$ is set to avoid singularities.

3 RESULTS – I. TURBULENT MASSIVE DISCS

The main result of this study is the formation of rotationally supported thick discs, characterized by supersonic turbulence and a moderately strong magnetic field. Fig. 2 shows snapshots for a grid of simulations illustrating the evolution of the pre-stellar cores inside turbulent GMCs. In all four simulated pre-stellar cores with various initial masses and morphologies, quasi-Keplerian discs form around the central proto-star/binary. The morphologies of the discs are very similar to those found in many previous studies (Bate, Bonnell & Bromm 2003; Goodwin, Whitworth & Ward-Thompson 2004a; Hennebelle & Fromang 2008): spiral arms that could potentially transport angular momentum are prominent features. We summarize the key properties of the discs in Table 1.

In the classical picture, the gravitational collapse of a magnetized pre-stellar core occurs from an initially spherical structure that tends to flatten along magnetic field lines, leading to the formation of an oblate pseudo-disc (Galli & Shu 1993). These pseudo discs are disc-like but are not supported by centrifugal force and may transition into centrifugally supported discs (Galli & Shu 1993; Joos, Hennebelle & Ciardi 2012). The collapse of TCs in our simulations spans a wide variety of morphologies (Fig. 2) that are far different from idealized spherical collapse.

Examples of spherical collapse geometry are cores *A-hr* and *C* in Fig. 2. In the second geometry, the core collapses into a thin elongated filament, which breaks into aligned quasi-spherical fragments. This fragmentation mode is represented by cores *B* and *D*. In the filamentary fragmentation the pre-stellar cores form from a larger-scale filament structure, hence they are aligned in one direction before reaching the centre of mass and become randomized. This is in contrast to the spherical collapse in which the core initial positions are already randomized during the fragmentation phase. Even in the spherical collapse geometry small filaments are visible but not aligned on large scales: the fragments form in hierarchical arms or bars probably due to the higher angular momentum of the gas in this mode of collapse. Regardless of the different modes of collapse, the outcome is a geometrically thick massive disc, in which the pre-existing fragments are collected (see Fig. 3). The orbiting fragments may lead to the formation of low-mass stars that are either ejected or spiral towards the centre.

The 5th, 6th, and 7th columns in Table 1 report the initial (when the core density reaches 10^6–10^7 cm^{-3}) kinetic, rotational, and magnetic energy compared to the gravitational potential energy of each core. We do not find any strong correlation between these initial properties of the cores and their subsequent collapsing mode. For instance, in the case of Core *B*, the core has initially large kinetic energy (high α_{vir}) and weak rotation (low β_{rot}), consistent with a strong radial infall along the arms, hence filamentary collapse. However, this interpretation fails to apply to Core *C* which similarly has large kinetic energy and weak rotational support but collapses in the spherical mode. We, therefore, do not find a strong connection between the aforementioned initial properties of the cores and their collapsing mode other than their initial geometry, as shown in Fig. 2. With only six cores reported in this work, we do not have enough statistics to comment on the probability of one mode over the other. At this time we simply conclude that different modes are primarily determined by the initial degree of elongation of the cores.

As the gas collapses and the density becomes higher than $\sim 10^6$–10^7 cm^{-3}, almost inevitably conservation of angular momentum produces quasi-Keplerian protostellar discs. Almost all the gas with density above 10^7 cm^{-3} is in discs rather than turbulent quasi-spherical cores (see Fig. 2). This is in contrast to the hierarchical structure of the molecular cloud at larger scales and lower densities, better described as clumps composed of more compact mini-clumps (see He et al. 2019). The cores in our zoom-in simulations have
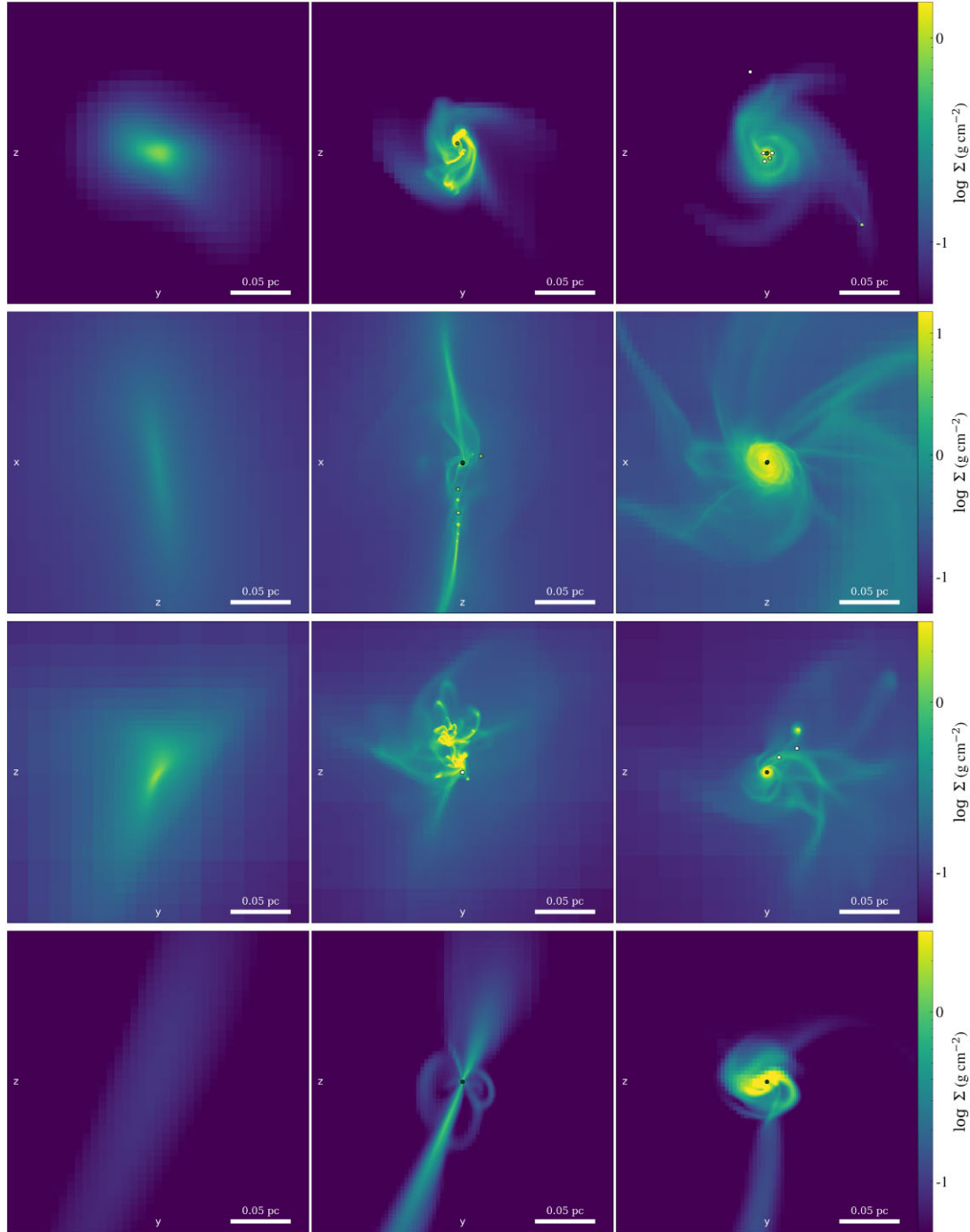
Figure 2. Gallery of the collapsing pre-stellar cores *A-hr*, *B*, *C* and *D*, from top to bottom, respectively. The colours are the column density of the gas in a direction aligned with the box but nearly parallel to the angular momentum direction of the gas. The first snapshot for each core shows its initial morphology and the second snapshot shows how the core collapses. The third snapshot is at a time when the disc reaches a quiescent, nearly steady-state phase. Sink particles representing single stars are plotted on top as coloured circles, with darker shades indicating higher masses. The cores display two distinct kinds of morphology. Cores *A-hr* and *C* are examples of a spherical mode of collapse, while Cores *B* and *D* are examples of the filamentary collapse mode. Note that the colourmap in the second row has a higher upper limit.

masses between $\sim$27 and $\sim$120 $M_\odot$, and the protostellar discs forming from their collapse are thick and supported in the vertical direction by magnetic pressure and turbulent pressure rather than thermal pressure. This is contrary to what is observed in simulations of standard lower mass protostellar discs around solar mass proto-stars, in which the disc scale height is determined by thermal pressure

(e.g. André Oliva & Kuiper 2020). We will discuss this result in detail in Section 3.3.

Apart from a central star/binary that eventually grows to have a large fraction of the total mass of the core, multiple secondary stars form at the outskirt of the pseudo-disc. These stars form from pre-existing fragments formed uniformly inside a quasi-spherical TCor
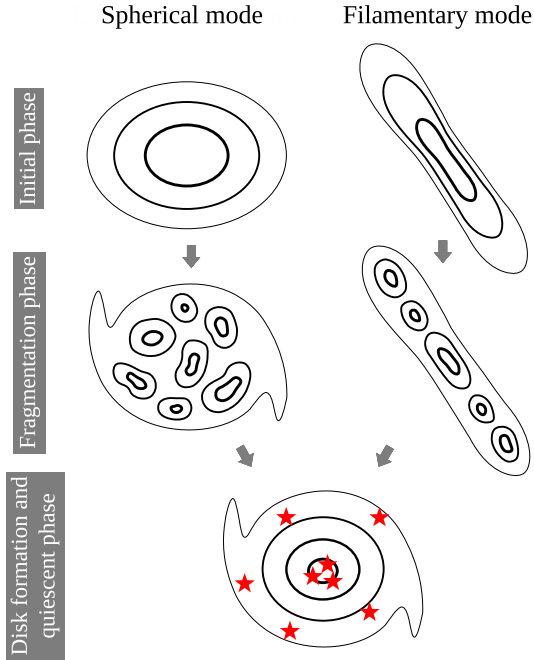
Figure 3. Schematic of the two modes of pre-stellar core fragmentation and disc formation. In the spherical mode, the core begins with a spherical/oblate shape and fragmentation occurs in arms, bars, or mini-filaments inside the core. In the filamentary mode, or mode B, the core starts from a long, thin tube and instabilities occur on the arms of the filament. In both scenarios, a centrifugal disc forms at the core centre a few hundred kiloyears after the initial phase. The discs have sizes up to several thousand au. The central star/binary and secondary stars that form from the core fragments orbit around the disc centre, entering a quiescent phase.

from the fragmentation of a collapsing filament. Shortly after their formation, some of these fragments spiral into the centre of the disc owning to either dynamic friction or torques exerted by accretion or gravity from the asymmetric core, and some are ejected from the system. In the last phase of the evolution, between 1 and 12 stars form in the core. This is consistent with previous numerical studies (Bate & Burkert 1997; Goodwin et al. 2004a, b). None the less, these small *N*-body systems are unlikely to be observed because they evaporate into the field on time-scales shorter than the lifetime of the discs. It remains to be understood whether the stars produced by the dissolution of this small hierarchical *N*-body system retain their original binary fraction.

In the rest of this section, we closely examine the properties of the centrifugal discs in cores *A-hr* and *B*, demonstrating that the disc's scale height is primarily determined by magnetic support and turbulent motions.

Let us first introduce some definitions useful to describe the stability of the cloud to fragmentation and the importance of the magnetic field.

The dynamical importance of the magnetic field in a cloud of mass M is often parameterized in terms of the dimensionless ratio $\mu \equiv M/M_\Phi$, where M_Φ is the magnetic critical mass: the mass at which the pressure from the magnetic energy, $\mathcal{B}$, balances the gravitational binding energy, $\mathcal{W}$, of the cloud. For a spherical cloud of uniform density and uniform magnetic intensity, $\mathcal{W} = -3GM^2/(5R)$ and $\mathcal{B} = B^2 R^3/6 = \Phi_B^2/(6\pi^2 R)$, where $\Phi_B \equiv \int B_\perp dS = \pi R^2 B$ is the magnetic flux. By setting $|\mathcal{W}| = \mathcal{B}$, we get the magnetic critical mass

$$M_\Phi = \sqrt{\frac{5}{2}} \frac{\Phi_B}{3\pi\, G^{1/2}}.$$ (2)

Then,

$$\frac{|\mathcal{W}|}{\mathcal{B}} = \frac{18\pi^2}{5} \frac{GM^2}{\Phi_B^2} = \frac{M^2}{M_\Phi^2} = \mu^2.$$ (3)

In our analysis, we adopt the equivalent definition $\mu = \sqrt{|\mathcal{W}|/\mathcal{B}}$ to calculate the mass-to-flux ratio in our simulations. The advantage is that it accounts for the inhomogeneity of the density and magnetic field distribution as well as the binding energy between the central stars and the disc. For a cloud or a core that is centrally concentrated, μ calculated using this definition is slightly higher than the classical definition because the binding energy is increased by the mass concentration in the centre.

Simulations (Joos et al. 2012) have shown that if $\mu \lesssim 1$, the cloud does not collapse due to the support of the magnetic field. If $1 \lesssim \mu \lesssim 5$ the cloud collapses but magnetic braking prevents the formation of a disc and the gas collapses quasi-spherically. If $\mu \gtrsim 5$ a quasi-Keplerian disc can form. We will show that in our simulations pre-stellar cores have $\mu \sim 1$–5; however, we nevertheless observe the formation of quasi-Keplerian discs.

Neglecting the effect of the magnetic forces, we define the Toomre Q parameter

$$Q = \frac{\Omega\, \sigma(v_z)}{\pi G \Sigma},$$ (4)

where we have replaced c_s with the vertical turbulent velocity $\sigma(v_z)$ since, as we will show later, the support of the disc against gravity in the vertical direction is dominated by turbulent motions rather than thermal pressure.

3.1 Evolution of a 27 solar mass core (Core *A-hr*)

In this section, we describe the properties of one of the smaller cores in our set of simulations: core *A-hr*. The general properties of this core are shown in Table 1, also showing that the resolution of this simulation is ∼7 au, the highest in our set. This core forms in the quasi-spherical geometry of fragmentation. Each panel in the top two rows of Fig. 4 shows the gas density on a slice through the centre of the core/disc and the smaller insert shows the projected gas density in a view parallel to the angular momentum of the gas (face-on, first row) and a view perpendicular to it (edge-on, second row). From left to right, each panel shows the time evolution of the core as indicated by the labels.

When the core starts collapsing it has a spheroidal shape; we define time $t = 0$ when the central density of the core reaches ∼10^6 cm^{-3}. In Fig. 4, the snapshots are shown at times $t = 0, 50, 200,$ and 400 kyr, from left to right. The last three snapshots correspond to times when: (i) a disc forms and becomes Toomre unstable at its centre; (ii) when the first star forms; and (iii) when a quasi-steady (quiescent) disc forms.

Due to the conservation of angular momentum, the spherically symmetric collapse transitions into a rotation-dominated but turbulent fragmentation. As the central density increases and the disc becomes more gravitationally (Toomre) unstable, a spiral arm forms at the centre of the core. The subsequent evolution of the core is crucially dependent on supersonic turbulence. Eddies of eddies emerge and dense sub-cores at their centres spiral inward. This is a well-known mechanism that allows rapid gas accretion and transport of angular momentum in an unstable disc. These dense blobs are the
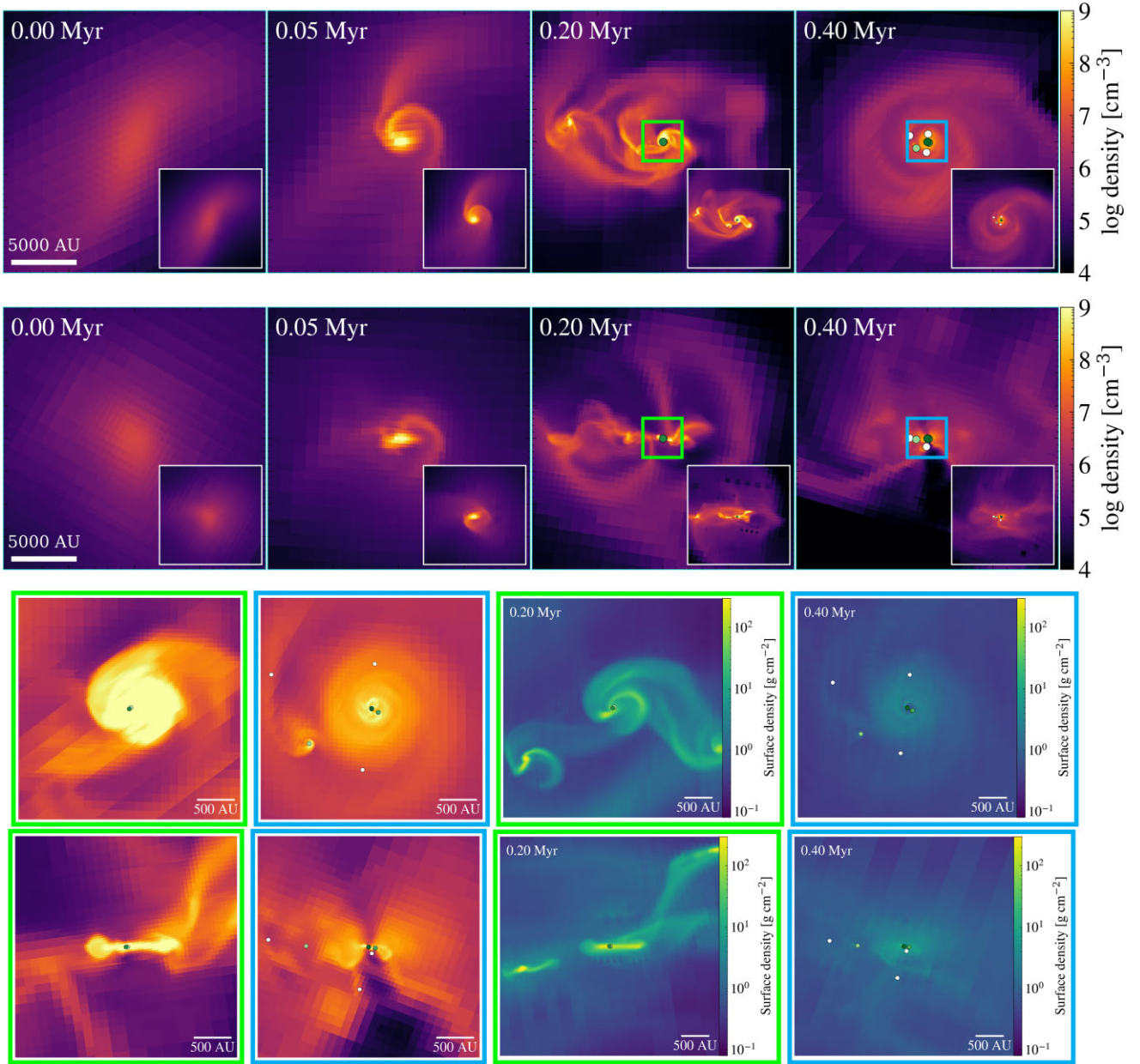
Figure 4. Density slices of the $\sim 27\,\mathrm{M_\odot}$ core (Core *A-hr*) at the mid-plane (first row) or cross-section (second row) at various ages. The images measure 2×10^4 au (~ 0.1 pc) on a side, and the circles mark the positions of the star particles with darker shades indicating higher mass. Density-weighted projections of the gas density are inserted at the bottom right corners of each panel to better demonstrate the core structure. The first snapshot is chosen at the initial isothermal phase when the central density reaches $10^6\,\mathrm{cm^{-3}}$. The second snapshot is picked when the instability occurs in the centre. The third snapshot is picked when the first stars form at the centre. The fourth snapshot is picked when the disc comes to a quiescent phase. The last two rows display a zoomed view of the disc which is characterized by volume density above $10^{8-9}\,\mathrm{cm^{-3}}$, or surface density above $\sim 10\,\mathrm{g\,cm^{-2}}$. The core spherically collapses from the initial sphere into a disc whose spiral arms could potentially transport angular momentum outward. A mini-cluster of stars orbits around the disc centre.

locations where later on a single-star or a multiple-star system will form. When the first star forms at the centre of the system, accretion of gas into the central star clearly appear as a protostellar disc with prominent spiral arms, similar to those seen in many previous studies (Bate et al. 2003; Goodwin et al. 2004a; Hennebelle & Fromang 2008). A zoom-in view of this smaller disc at times 200 and 400 kyr is shown in the last two rows of Fig. 4. The first two columns show the gas density in a slice through the disc face-on (third row) and edge-on (fourth row) to emphasize the typical flared shape of the disc in the edge-on view. The last two columns show the gas surface density,

emphasizing the presence of spiral arms and the presence of other smaller discs forming from the contraction of other nearby smaller fragments, in good agreement with recent observations discussed above.

In Fig. 5, we show a detailed quantitative characterization of the time evolution and properties of the collapsing core leading to the formation of the disc. We consider either spherically averaged profiles, most appropriate to describe the initial phases of the evolution and the outer parts of the core that maintain quasi-spherical geometry, or cylindrical coordinates, most appropriate to describe the
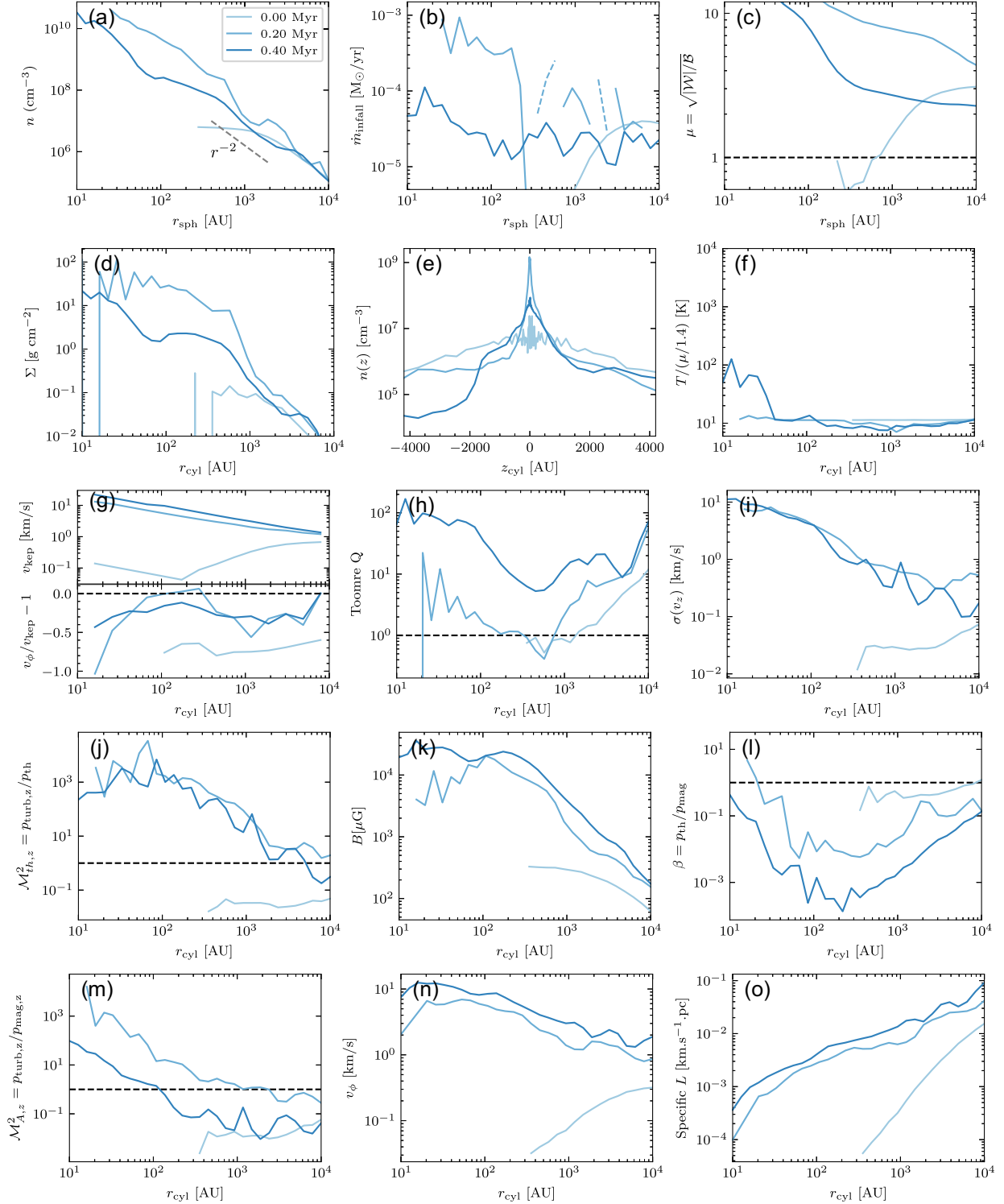
Figure 5. Radial and vertical profiles of the 27 M$_\odot$ core *A-hr*. The *x* axis represents the radius in a spherical coordinate r_{sph}, i.e. the distance to the centre, or the radial distance in a cylindrical coordinate r_{cyl}, or the longitudinal position z_{cyl}. The curves are averaged values of the following physical quantitates: (a) Number density at spherical radius r_{sph}. (b) Mass infall rate at r_{sph}. The dashed curve indicates a negative infall rate. (c) Mass-to-flux ratio at r_{sph}, defined as the square root of the ratio of gravitational binding energy to magnetic energy, $\beta = \sqrt{\mathcal{W}/\mathcal{B}}$, enclosed within r_{sph}. This is equivalent to the common mass-to-critical mass definition. (d) Column density at cylindrical radius r_{cyl} in a depth of 5000 au. (e) Number density of a cylinder with radius 6000 au at cylindrical height z_{cyl}. (f) Temperature at r_{cyl}. (g) Non-Keplerianity on the disc plane defined as $(v_\phi - v_{kep})/v_{kep}$. (h) Toomre Q at r_{cyl}. (i) Vertical-component velocity dispersion at r_{cyl}. (j) Square of *z*-component thermal Mach number, $\mathcal{M}_{th}^2 = p_{turb,z}/p_{th}$ at r_{cyl}. (k) Magnetic field strength at r_{cyl}. (l) Plasma beta, $\beta = p_{th}/p_{mag}$, at r_{cyl}. (m) Square of the *z*-component Alfven Mach number, $\mathcal{M}_A^2 = p_{turb,z}/p_{mag}$, at r_{cyl}. (n) Disc's azimuthal velocity as a function of r_{cyl}. (o) Disc's specific angular momentum as a function of r_{cyl}.

disc structure. The origin of the coordinate system is set at the centre of the disc or core. For the cylindrical coordinate system, the z-axis is set along the direction of the angular momentum of the gas. The different lines show the profiles at times corresponding to the three times shown in the legend, which also corresponds to the 1st, 3rd, and 4th columns in the top two rows of Fig. 4, with an increasing shade of darkness indicating later times in the evolution.

1. **Evolution and structure of the collapsing core and the disc.** Panel (a) shows the density profile of the gas in spherical coordinates, $n(r_{sph})$. At the time $t = 0$, the core can be approximated by an isothermal cloud in hydrostatic equilibrium, showing a Bonnor–Ebert density profile with a central density 6×10^6 cm^{-3} and core radius $\sim$900 au. The envelope of the isothermal sphere extends up to 0.25 parsec (5×10^4 au), despite being beyond the range of the x-axis and not visible in the figure. The collapsing core has an enclosed mass of $\sim$27 M$_\odot$ within 0.25 parsec, or above a density of 3000 cm^{-3}. The density of the isothermal core increases self-similarly as the core collapses and reaches a density of 5×10^9 cm^{-3} before a protostar (sink particle) forms at the centre. The density profile has a power-law slope of about -2 in the outskirt of the core, consistent with an isothermal sphere in hydrostatic equilibrium. The net mass infall rate (panel b) is between 10^{-5} and 10^{-4} M$_\odot$ yr^{-1} and the total accreted mass into the centre is about 17 M$_\odot$ by the end of the simulation at $t = 0.4$ Myr.

At the time $t = 0$ the core is marginally magnetically supercritical as shown in panel (c): μ ranges from 0.6 to 3 from the inner region to the outer region. Over time, as the mass accumulates into the central stars in a compact region, the gravitational binding energy increases dramatically while the magnetic energy does not increase as rapidly, due to the decoupling of the magnetic fields from gas as a result of star formation. We will discuss the properties of the magnetic fields and the disc formation in follow-up work.

The remaining panels show the properties of the pseudo-disc in cylindrical coordinates. Panel (d) shows the face-on surface density profile of the disc, which increases from 1 g cm^{-2} at $r_{cyl} = 10^4$ au to 10–100 g cm^{-2} at the centre. This surface density is comparable to what is observed in Class II discs around young stellar objects in Ophiuchus (e.g. Andrews et al. 2009).

The density profile of the disc in the vertical (z-axis) direction $n(|z|)$ (the average of z and $-z$) is shown in panel (e). The disc thickness is 400–500 au at a threshold density of 10^7 cm^{-3} at times $t > 200$ kyr. At the same mean density cutoff, the radius of the disc is roughly 1000–2000 au, therefore the disc is rather thick with an aspect ratio $H/R \sim 1/2 - 1/4$.

The average gas temperature in the disc (panel f) remains near 10 K throughout the simulation. In the centre of the disc after the formation of the first star, the gas temperature increases to $\sim$100 K as a result of photoionization heating from massive stars. As will be discussed in Section 5.2, the ionizing UV radiation from the stars at these early times is trapped in the thick dense disc and the disc remains cold at radii >100 au in most simulations.

2. **Keplerianity and stability of the disc.** The disc has a quasi-Keplerian rotation, with a deviation from Keplerianity $\beta_{kep} \equiv (v_\phi - v_{kep})/v_{kep}$ of the order 50 per cent (see bottom of panel g). The deviation is mainly due to the relatively large accretion rate of gas: as shown in panel (b), where and when the mass accretion rate is higher, corresponds to a larger deviation from Keplerianity. In addition, both the radial infall rate and the deviation from Keplerianity are larger when the disc is more strongly gravitationally unstable as illustrated in panel (h) showing the profile of the Toomre Q parameter. The pseudo-disc starts more strongly gravitationally unstable ($Q < 1$) and transitions into a stable disc after about 0.3 Myr from $t = 0$.

3. **Turbulent, thermal, and magnetic support of the disc.** The disc is very turbulent: the turbulent velocity in the vertical direction, $\sigma(v_z)^2 = \langle v_z^2 \rangle - \langle v_z \rangle^2$, is between 1 and 10 km s^{-1} (panel i) and the turbulence is highly supersonic as shown by the square of the thermal Mach number in the vertical direction (or the ratio of the turbulence pressure over the thermal pressure in the z-direction) shown in panel (j). The core starts with negligible turbulence, supported by thermal pressure. The pseudo-disc phase is instead dominated by turbulence motions, with rms velocity in the z-direction of about a third of the Keplerian velocity and significantly higher than the sound speed of the gas ($c_s \sim 0.3$ km s^{-1}), reaching Mach numbers of 10–30. Hence, we expect a geometrically thick disc supported by supersonic turbulent motions, as discussed in more detail in Section 3.3.

The core is magnetized with an initial magnetic strength of about 50–300 μB (panel k). The magnetic field is amplified by the accretion of gas and increase of the surface density of the gas, which can be partially explained owing to magnetic flux freezing, i.e., $\mu \propto M/\Phi_B = \Sigma/B \sim$ const. The turbulence also grows dramatically due to non-axisymmetric collapse, despite the existence of relatively strong magnetic fields. During this process, the core transitions from a thermal and magnetic pressure-dominated phase into a turbulent pressure-dominated phase (panels j and l), with a plasma β as low as 10^{-2} at a few 100 au and thermal Mach number as high as 10–10^2 in the inner region (<100 au). Finally, in the quasi-steady phase of the disc, the turbulent pressure in the inner parts of the disc still dominates over the magnetic pressure but this is reversed at radii $r_{cyl} \gtrsim 100$ au (see panel m).

4. **Analysis of velocity gradients in comparison to observations.** In this part, we analyse this simulation with the objective of comparing it to observations in terms of the velocity gradients and specific angular momentum and discuss whether or not our simulations successfully reproduce some features of the observations.

In an axis-symmetric model with initial rotation, the angular momentum measured at various scales is perfectly aligned.

We analyse the magnitude of the angular momentum in our simulated disc and its alignment at various scales. We consider a cylinder of height $h = 500$ au centred by the disc and aligned with the spin axis of the disc. The average specific angular momentum are measured to be 4×10^{-3} and 1.5×10^{-2} km s^{-1} pc, measured within $R = 800$ au, the radius of the disc, and $R = 5000$ au, enclosing the envelope, respectively. These values are consistent with observations of the protostellar regime from the CALYPSO data set ($j \sim 10^{-3}$ km s^{-1}, see Belloche 2013; Gaudel et al. 2020 and the citations therein). The specific angular momentum as a function of distance to the centre (panel o of Fig. 5) also follows the power-law relation $j \propto r^{1.6-1.7}$, highly consistent with observations of Class 0 envelopes (Goodman et al. 1993; Caselli et al. 2002). The relative angle between the angular momentum measured at two scales is 12°. This misalignment is largely due to the turbulence of the initial core. This is in agreement with Verliat et al. (2020), who find that the formation of a disc can be a result of small perturbations of the initial density field in the core in the absence of large-scale rotation.

Panel (n) in Fig. 5 displays the azimuthal velocity at various distances. We see a transition from the inward velocity gradient in the initial core to the outward velocity gradient of the disc and envelope, which indicates an evolution from a slowly rotating rigid body (*i.e.*, nearly constant angular velocity) to a differentially rotating Keplerian disc. The amplitude profile of the velocity gradient, or the angular velocity with respect to the disc centre, roughly follows a power law $\Omega \sim r^{1.4}$, close to that of a Keplerian disc with all the mass concentrated at the centre, which gives $r^{-1.5}$. These features can be tested with observations of molecular lines in nearby star-forming
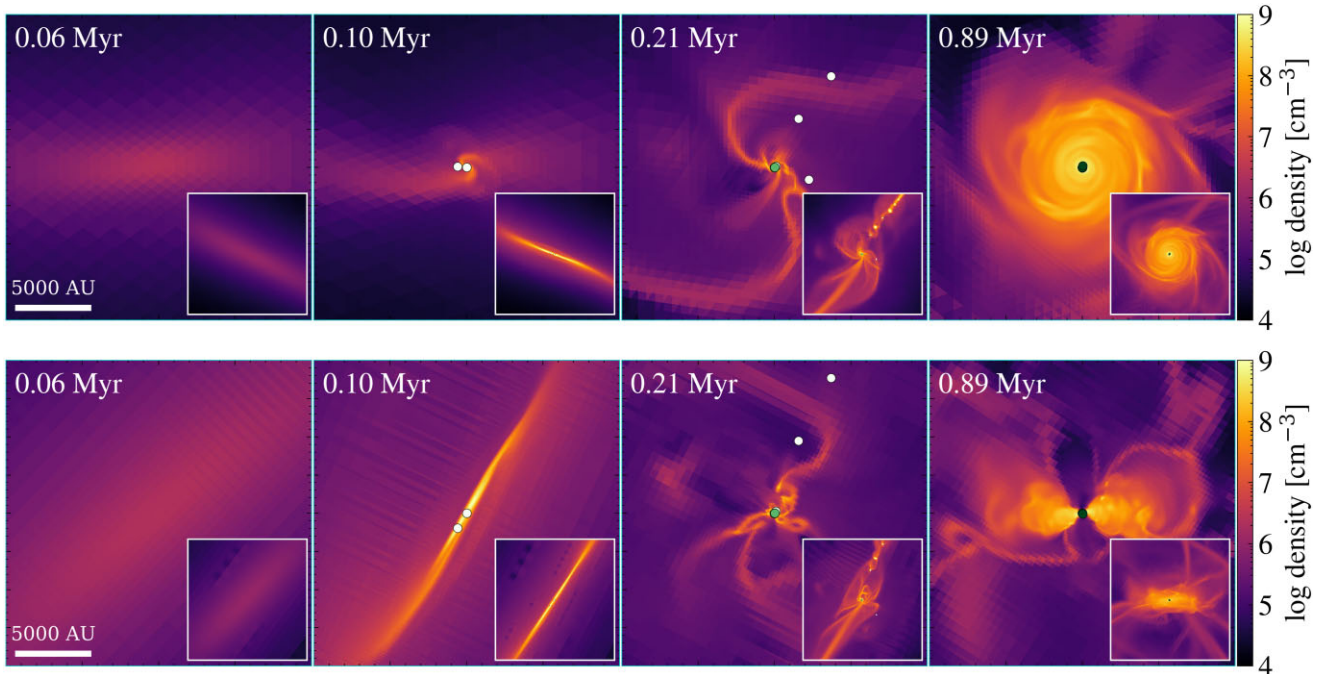
Figure 6. Same as Fig. 4 but for the very massive core (Core *B*). Starting from a thin tube, the core undergoes fragmentation at the centre as well as along the arms of the cylinder. With large feeding of gas along the filament, the central stars grow in mass rapidly, ending in a total mass of over 600 $M_\odot$. The gas keeps feeding the central stars via a large, thick disc, tens of solar masses in mass.

regions which can measure velocity gradients in the cores (at large scales) and in the discs (at smaller scales) with a precision of about 1 km s^{-1} pc^{-1} (e.g. Cheng et al. 2022), which is sufficient to detect the slow rotation (at subsonic/sonic speeds) of cores out to 10 000 au scales.

3.2 Evolution of a 130 solar mass core

The properties of core *B*, a very massive core that grows from 130 $M_\odot$ to a mass of over 600 $M_\odot$, are qualitatively similar to core *A-hr* once we account for the fact that it is much more massive. In this section, we will emphasize the differences between this core and the less massive core *A-hr* discussed above. Fig. 6 shows the projected density distributions of the core from face-on (top) and edge-on (bottom) views, as in Fig. 4.

Unlike core *A-hr* which collapses spherically, core *B* starts from the collapse of a filamentary structure and fragments along the length of the filament. This filamentary collapse of a massive core is observed in recent ALMA continuum maps at mm wavelength of a highly magnetized clump (Fontani et al. 2016). However, the final outcome of the collapse is a disc similar to the case of core *A-hr*, although much more massive. At the time $t = 0$ the initial density structure is better described by a cylindrical geometry than a spherical core (see the first and second frames in Fig. 6). The fragmentation of the core starts at the centre of the frame where the density is highest. As the density reaches 10^9 cm^{-3}, the Jeans length drops to a few hundred au and the local free-fall time is a few kyr. The filament undergoes fragmentation along the length of the cylinder and breaks into blobs that become eddies (the third frame). Finally, these eddies migrate into the centre of the system in about one dynamic time. Conservation of angular momentum turns the filamentary collapse into rotational collapse, forming a large, thick disc (the last frame).

We plot the properties of this filament/disc as a function of time in Fig. 7, with timestamps corresponding to the four snapshots in Fig. 6.

Even though the geometry of the core at $t = 0$ is not spherical but filamentary, the spherically averaged density profile is well described by a Bonnor–Ebert density profile with a central density 2×10^6 cm^{-3} and core radius $\sim$2000 au (panel a). Between 0.1 and 0.4 Myr, the radial distribution of density displays a power-law profile with an exponent close to -1.5, which is flatter than an isothermal sphere, likely because the geometry is clearly filamentary at these times. After $\sim$0.4 Myr, the core exhibits a nearly constant density profile with $n \sim 10^7$ cm^{-3} within 4000 au, indicative of a disc with nearly constant density and constant surface density as shown in panel (d). This disc is about 4 times larger than disc *A-hr* at the same density threshold, but disc *A-hr* has an increasing density and surface density towards the centre. By $t = 0.9$ Myr (the dark blue curve), a large, thick, near-Keplerian disc forms with a surface density of $\sim$10 g cm^{-2}. The radius of the disc is about 4000 au at a cutoff density 10^7 cm^{-3}, equivalent to a column density of 3 g cm^{-2} (panel d). Within this radius, the disc is near Keplerian (panel g) and at late times is Toomre-stable ($Q > 1$, see panel h): even though in the outer parts $Q \sim 1$ we do not observe late time fragmentation probably due to the stabilizing effect of magnetic fields. The thickness of the disc is about 2000 au at the same cutoff density of 10^7 cm^{-3} (panel e).

Unlike disc *A-hr* where the radial component is extremely turbulent and the mass inflow is discontinuous, disc *B* has a steady inflow at a constant velocity of 2–3 km s^{-1}, which is close to the escape velocity at the edge of the disc at 5000 au from the centre. With a $\rho \sim r^{-2}$ relation, the inflow of mass has a constant rate 3×10^{-4} $M_\odot$ yr^{-1} (panel b). This inflow rate results in an accreted mass of >400 $M_\odot$ in the accretion period of 0.5 Myr.

Due to the large central mass, the Keplerian velocity of the disc is high, reaching 7–20 km s^{-1} at 1000 au. The turbulent velocity
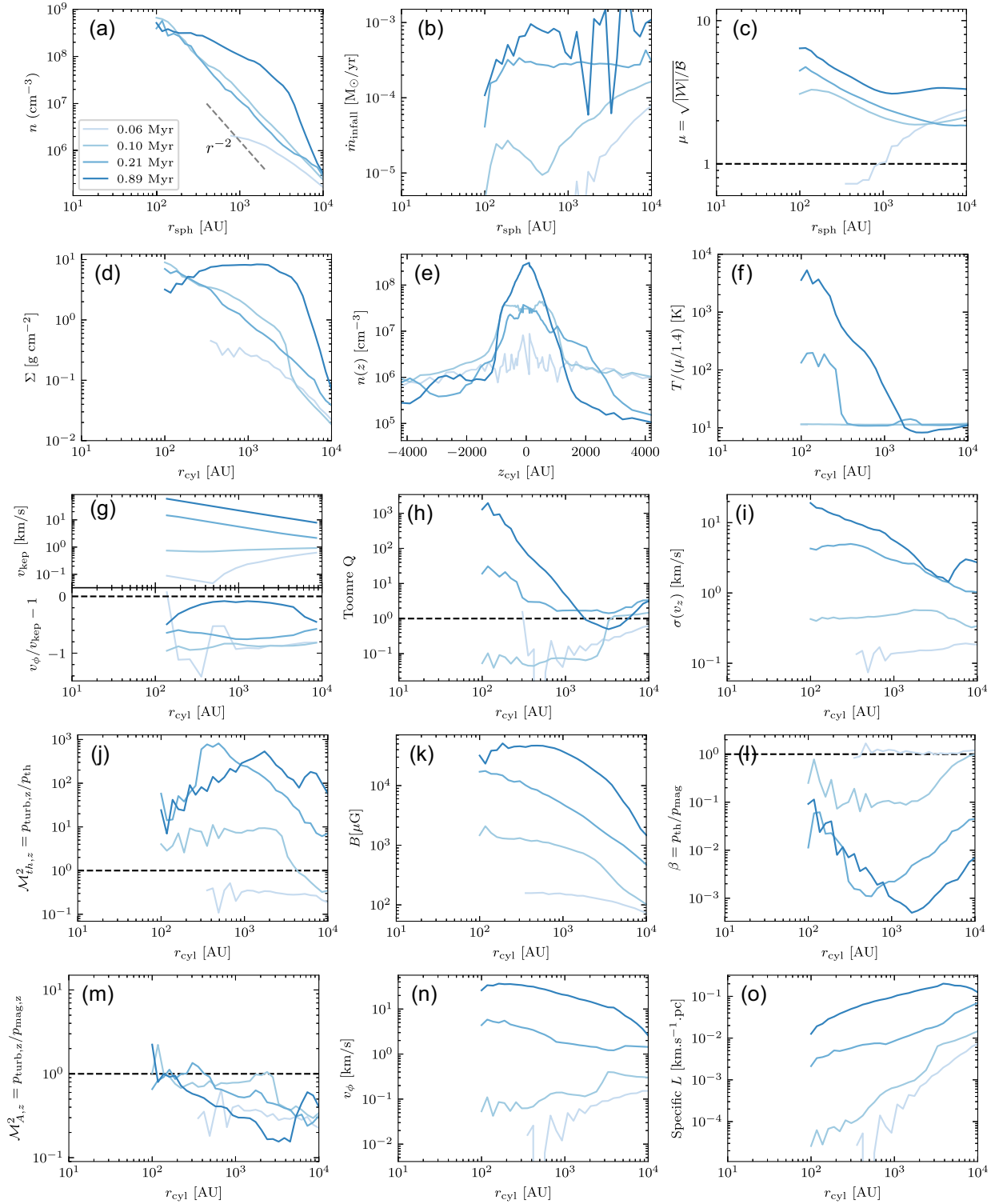
Figure 7. Same as Fig. 5 but for the $\sim 130\,\mathrm{M}_\odot$ core B. Refer to the texts for the implications and interpretations.

is also very high, between 3 and 6 km s^{-1} in the z component (panel i).

Due of magnetic flux freezing, the large mass in the disc results in large magnetic strength, reaching between 10^3 to $5 \times 10^4\,\mu$G (panel k). Despite of the strong magnetic field, the mass-to-flux ratio μ stays high between 3 and 7 (panel c) due to the large gravitational binding

energy from the large mass of the cluster at the centre. Although the inner part of the disc is heated by UV radiation to 100–3000 K (panel f), the disc is supported primarily by magnetic pressure and secondarily by turbulence in the axial direction (see panels j, l, and m). We will discuss the support of the disc in more detail in the next section.
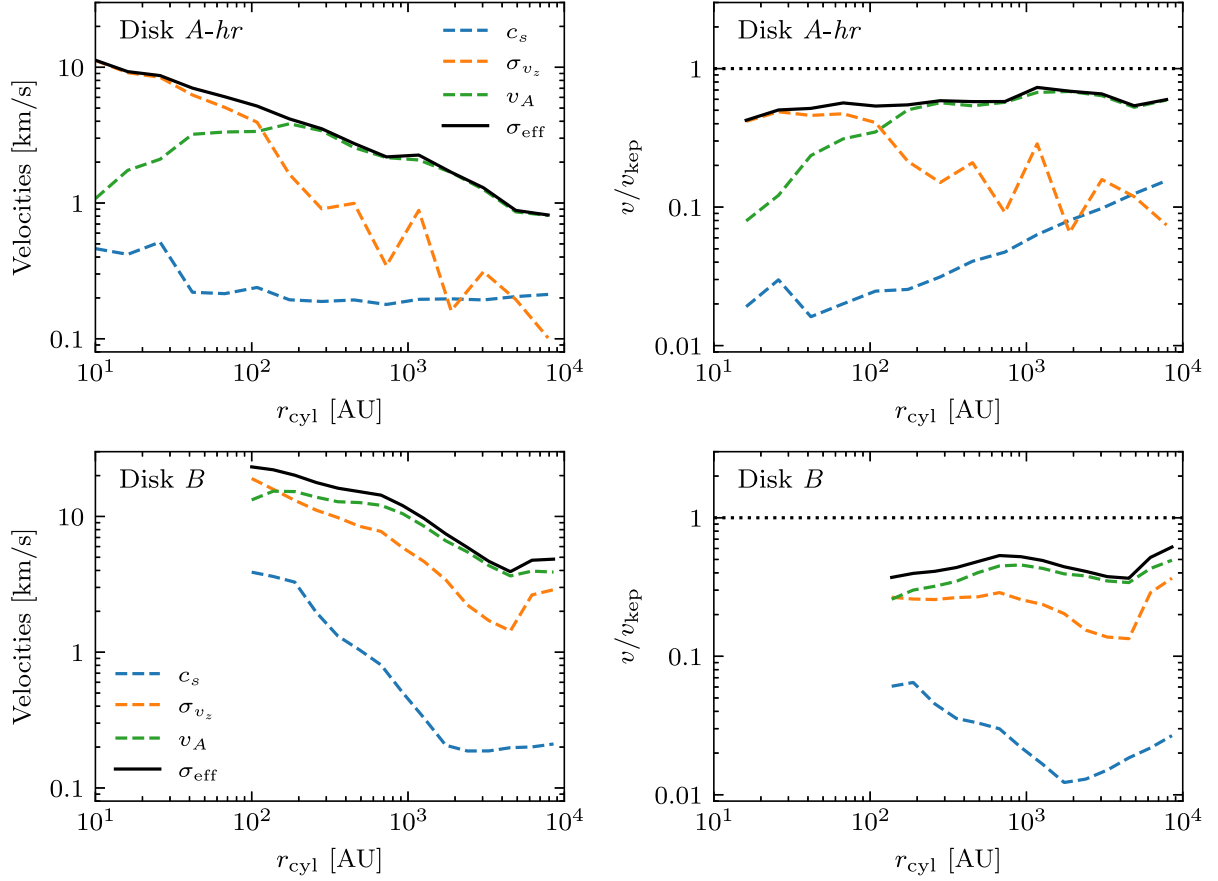
Figure 8. (*Top*) Left-hand panel: Radial profiles of the sound speed (dotted–dashed line), the Alfven speed (dashed line), and the z-component turbulent velocity (rms velocity in the z-direction, solid line) for our lower-mass disc (Disc *A-hr*). Right-hand panel: the same quantities normalized to the Keplerian velocity $v_{\rm kep}$. This ratio reliably predicts the scale height H/r of a gas disc in hydrostatic equilibrium, where the vertical component of gravity is balanced by the pressure ρv^2 gradient. The panels illustrate that the vertical support of the disc is dominated by turbulence and by the magnetic field, while thermal pressure support is negligible. The right-hand panel also shows that $\sigma_{\rm eff}/v_{\rm kep} \sim 0.5$, and hence the disc is geometrically thick, i.e., the disc has an aspect ratio of about 0.5. (*Bottom*). The same as the top panels but for our most massive disc (Disc *B*). We note that in both discs the turbulent support dominates from the centre to 200 au and the magnetic support from $r_{\rm cyl} \sim 200$ to $\sim 10^4$ au.

3.3 The discs thickness is determined by magnetic support and supersonic turbulent motions

The discs in the six simulated cores measure from 200 to 6000 au in radius, with Disc *B* being the largest and most massive one. They are generally very thick as well, mostly with an aspect ratio (thickness to diameter ratio) of 0.2–0.5. Here, we explore the physics behind the existence of these large discs.

For a disc of gas around a massive central object that is in hydrostatic equilibrium with the z component of gravity from the centre,

$$\frac{dP}{dz} = -\frac{GM\rho z}{(r^2 + z^2)^{3/2}} \approx -\frac{GM\rho z}{r^3}. \tag{5}$$

where r is the radial cylindrical coordinate for the distance from the centre and z is the altitude cylindrical coordinate for the distance from the disc mid-plane. Assume the pressure P can be expressed as $P = \rho\langle v^2\rangle$, then

$$\langle v^2\rangle \frac{d\rho}{dz} = -\frac{GMz}{r^3}\rho, \tag{6}$$

therefore

$$\rho = \rho_0 \exp\left(-\frac{v_\phi^2 z^2}{2\langle v^2\rangle r^2}\right) = \rho_0 \exp\left(-\frac{z^2}{H^2}\right), \tag{7}$$

where $v_\phi = \sqrt{GM/r}$ is the Keplerian velocity and H is the disc scale height,

$$H/r \approx \frac{\sqrt{2}\,\langle v^2\rangle^{1/2}}{v_\phi}. \tag{8}$$

The rms velocity $\sigma_{\rm eff} \equiv \langle v^2\rangle^{1/2}$ should account for all the possible pressure supports: thermal, turbulent, or magnetic. These three components can be identified as the sound speed c_s, the dispersion (rms) of the z-component velocity σ_{v_z}, or the Alfven speed v_A, respectively. We compare these three velocities and $\sigma_{\rm eff} = (\sigma_{v_z}^2 + v_A^2 + c_s^2)^{1/2}$ as a function of r in Fig. 8. It is clear that turbulent pressure dominates the vertical support of the disc in the inner disc and magnetic pressure dominates in the outer disc, while thermal pressure support is negligible everywhere. For the two discs shown in Fig. 8, the transition from turbulent support to magnetic support occurs at ~200 au. However, in another disc, we observed the transition radius to be closer to 1000 au. We will further investigate the dependence of the critical radius on the physical parameters of the core in future work.

We notice that σ_{v_z} decreases with the distance to the centre with an empirical relation $\sigma_{v_z} \sim r^{-0.6}$, while v_A peaks at $r_{cyl} = 200$ au and decreases slowly outward. The effective rms velocity σ_{eff} scales with radius as $\sigma_{eff} \sim r^{-0.5}$. Assuming a roughly Keplerian azimuthal velocity profile $v_{kep} \sim r^{-0.5}$, we have $\sigma_{eff}/v_{kep} \sim r^0$. The predicted disc aspect ratio H/r according to equation (8) is nearly constant as a function of radius and of the order of unity, as shown in the right-hand panels of Fig. 8. Assuming an isothermal density profile $\rho \propto r^{-2}$ as for disc *A-hr*, the disc surface density is $\Sigma \propto r^{-1}$, while disc *B* has $\rho \propto r^{-1}$ and a nearly constant surface density profile, $\Sigma \sim \text{const}(r)$. Indeed the discs have nearly constant opening angles and the surface density profiles we derived above are consistent with the actually geometrical properties of the discs shown in the fourth column of Figs 4 and 6.

The magnetic field plays a more significant role in determining the structure of the outer disc. At large radii ($\gtrsim 200$ au in both disc *A-hr* and disc *B*) the magnetic pressure dominates over turbulent pressure. Even though the initial strength of the magnetic field (10–$25\,\mu$G) of the cloud at density $10^3\,\text{cm}^{-3}$ is in the typical range of what is observed in present-day molecular clouds and the initial velocity dispersion is 5 times higher than v_A, the strengths inside both discs are above $1000\,\mu$G and even stronger at the very centre. The Alfven velocity is between 1 and $4\,\text{km s}^{-1}$ in Disc *A-hr* and between 4 and $15\,\text{km s}^{-1}$ in Disc *B*, many times higher than the thermal sound speed. Therefore, we expect that the magnetic field could become dominant dynamically over turbulence even in the inner parts of the disc in simulations with mildly stronger initial values of the magnetic field. We will explore this possibility in a follow-up work.

In our simulations, the gas temperature is underestimated near sources of radiation due to neglecting heating processes important at high densities (i.e. gas heating from stellar radiation absorbed by dust grains). With a more complete description of stellar feedback, the gas temperature could reach a value between 20 and 100 K at $n \sim 10^8\,\text{cm}^{-3}$ (Krumholz et al. 2007, 2011), corresponding to a sound speed of up to $0.9\,\text{km s}^{-1}$. Nevertheless, even assuming these higher temperatures, the thermal pressure is still small when compared to the turbulent and magnetic pressures found at these densities in our simulations. Thus, we speculate that even though we have neglected gas heating from dust grains, the enhanced thermal pressure support that this process provides should not play an important role in determining the structure of the disc and the protostars, at least for the massive cores studied in this work.

4 RESULTS – II. LOW-MASS STARS FORM FROM THE FRAGMENTATION OF MASSIVE PRE-STELLAR CORES

4.1 Fragmentation into low-mass stars before the formation of a steady disc structure

In the classical picture of pre-stellar disc formation, an unstable disc undergoes fragmentation and stars likely form from the disc fragments (Agertz et al. 2007; Kratter & Lodato 2016). Recent simulations of Pop III star formation (Machida et al. 2008; Stacy, Greif & Bromm 2010; Sugimura & Ricotti 2020; Park, Ricotti & Sugimura 2021a, b, 2023) clearly show that HM stars in a metal-free gas disc, although they form near the centre of the disc, which is most gravitationally unstable, nearly all of them migrate outward due to accretion of gas with higher specific angular momentum from the disc (but see also Chon & Hosokawa (2019), reporting exceptions to this behaviour for small mass fragments).

However, although we recognize a few low-mass disc fragments in our simulations, we find that steady quasi-Keplerian discs form only after the initial collapse and fragmentation phase of the cores: when clear disc morphologies can be identified these discs are relatively Toomre-stable.

André Oliva & Kuiper (2020) characterize the temporal evolution of protostellar discs starting from idealized initial conditions into four epochs: the initial setup, the disc formation epoch, the fragmentation epoch, and the quiescent epoch. In our simulations, we also identify four phases of the core evolution: the quasi-hydrostatic phase, the core fragmentation phase, the disc formation phase, and the steady-state (quiescent) phase.

In core *A-hr*, almost all of the self-gravitating fragments in which a star or a multiple stellar system forms, originate from high-density perturbations that appear and grow during the quasi-spherical collapse phase of the core, well before the formation of the pseudo-disc, as shown in Fig. 9. Keeping in mind the caveat that our discs are generally more massive than those in André Oliva & Kuiper (2020), the main qualitative difference between these two sets of simulations is that in the present work the fragmentation epoch precedes the disc formation phase. In other words, the formation of low-mass (disc) stars is initiated during the fragmentation of the core and before the disc formation phase. These phases are discussed in Section 3, and illustrated in Fig. 3.

A more realistic model of star formation from core fragmentation should take into account accurate modelling of stellar evolution. In our simulations, the formation time of protostar particles is instantaneous when a clump centre exceeds a given density threshold (see Section 3 for details on the sink formation criteria in RAMSES-RT (Bleuler & Teyssier 2014)). More realistically, the formation of protostars follows a thermal time-scale, or the Kelvin–Helmholtz (KH) time-scale. This time is extremely short for massive stars. For a low-mass star, say a solar-mass star, even though the KH time-scale is about 30 Myr long, the protostar shrinks to 100 solar radii, or about 0.5 au, by 1/100 of the KH time, or 0.3 Myr, assuming a constant rate of radiating thermal energy. This means that in a very short time after sink particle formation, a star becomes a subgrid particle in the simulation, well-tracked by a point-source sink particle.

The *N*-body integrator in the code uses a softening length of $2\Delta x_{min}$, which is 14 au for Core *A-hr* and 120 au for Core *B*. As a consequence, the formation of hard binaries is not captured and their dynamical evolution is not accurately resolved. We leave a robust treatment of the dynamics of these multiple systems for future work.

4.2 Star formation efficiency in cores and multiplicity

The observed core mass function (CMF) closely resembles the stellar IMF but is shifted to the higher mass end by a factor of ~ 3 (e.g. Alves, Lombardi & Lada 2007). This similarity seems to suggest the idea that the efficiency of star formation in dense cores ($n > 10^4\,\text{cm}^{-3}$) is of the order of 30 per cent. Previous studies tend to explain this offset invoking feedback, namely, protostellar outflows acting on core scales, entraining and expelling a large fraction of the core (Hansen et al. 2012; Kuiper, Turner & Yorke 2016). Numerical simulations (Kuiper et al. 2010; Offner & Chaban 2017) of isolated core-collapse suggest outflows have a mass-loading factor of ~ 3. In He et al. (2019), we instead argue that cores have close to 100 per cent star formation efficiency (SFE) but the cores fragment into several smaller mass stars with a relatively flat IMF. We show that such a model can reproduce both the shape and normalization of the IMF in our MC scale simulations, which we refer to here as 'baseline'
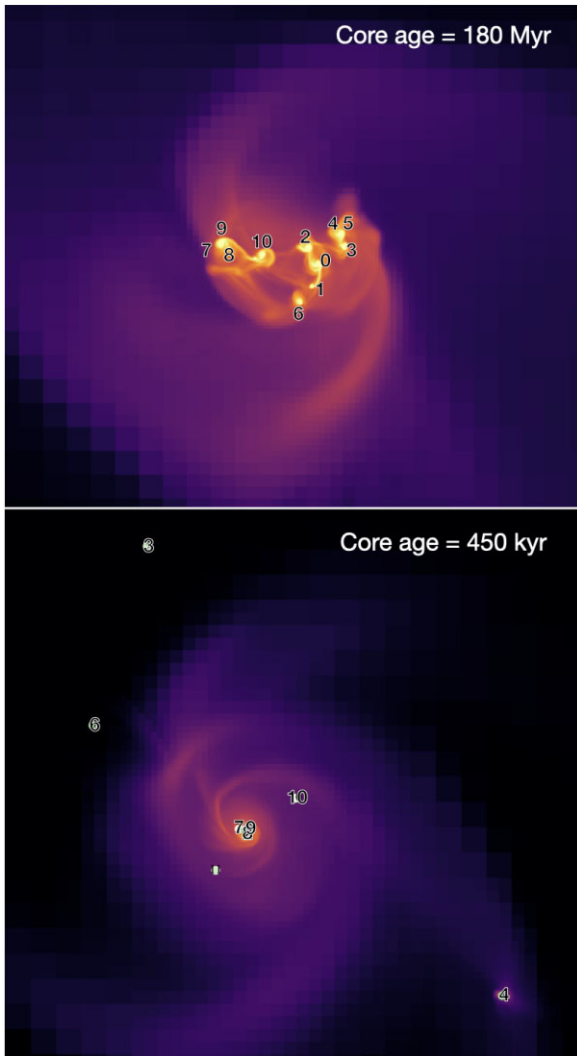
Figure 9. Snapshots of projected density of core *A-hr* after 180 kyr (*top*) and 450 kyr (*bottom*) from the isothermal core formation (defined as when the core density reaches 10^6 cm^{-3}). In the top panel, we identify the positions of the pre-stellar cores where sink particles form at later times, and show the IDs of the sink particles that form in them. In the bottom panel, the circles and numbers indicate the locations and IDs of the sink particles existing at the time shown in the snapshot. The figure shows that most sinks form from the fragmentation of a turbulent disc at an early time, but the sinks form with a time delay, and they either spiral in towards the centre of the disc or are ejected (or in the process of being ejected). The image measures 2×10^4 au on a side.

simulations. One of the main motivations of this work is to test this hypothesis by zooming on a few selected cores with high resolution.

Fig. 10 shows the mass function of the stars forming in each core in our simulations. The mass functions are plotted in two colours to distinguish the central stars (orange) from the companion stars (green). Black histograms are used when these two groups of stars are indistinguishable. We can see that each core fragments into a mini cluster consisting of 1–12 stars, as found in previous numerical studies (Bate & Burkert 1997; Goodwin et al. 2004a). In each panel, we compare the stellar masses in our zoom simulations to the sink masses of the 'baseline' lower resolution simulation of the same core, shown in the lower half of each panel. In the zoom-in simulations the spatial resolution increases by a factor ∼20 (∼60 for core *A-hr*),

reaching densities 3 orders of magnitude larger with respect to the baseline.

The labels in each panel of Fig. 10 compare the total stellar masses in the zoom-in simulations to the corresponding sink mass (representing a pre-stellar core) in baseline simulations. We find that the total masses of stars in the zoom-in simulations are either equal to or higher than the sink mass in the baseline, indicating that star formation efficiencies in cores are close to 100 per cent, independent of the core mass. In addition, we find that the cores in the zoom-in simulations have nearly 100 per cent efficiency of conversion of gas into stars: i.e., the final mass in stars is between 50 and 100 per cent the initial core mass, and for core *B* the mass in stars is higher than the initial core mass. However, the core forms multiple stars with the masses of the highest mass stars reduced by approximately 1/3. Hence, we argue that the CMF/IMF scaling parameter is due to the fragmentation of the core into multiple smaller mass stars rather than the inefficient conversion of gas into stars due to feedback effects. However, most of the mass in stars is locked in a few (2–3) relatively massive stars at the center of the disc, while low-mass stars – that can be numerous, e.g. core *A-hr* forms a total of 12 stars – account for a minority of the total mass of the core. Regardless of the mass of the fragments, the central stars accrete gas rapidly and grow in mass, contrary to disc star that instead remain of small mass, especially if they are ejected from the disc. Note that after sink particles are formed, they are not allowed to merge. Due to the small-number statistics, we cannot infer a shape for the mass function of stars in cores, but it appears to be flat. Additionally, the lack of proper treatment of protostellar outflow could result in an overestimation of the SFE in cores. A more rigorous study of feedback mechanisms in zoom-in simulations is necessary to better understand the SFE at these scales.

Recent studies have painted a picture of star formation as a highly dynamic process, replacing the idea that cores evolve slowly via ambipolar diffusion with one in which cores form in converging flow within a highly turbulent molecular cloud (Elmegreen 2000; Elmegreen & Scalo 2004). Goodwin et al. (2004a) suggest that low levels of turbulence (i.e. $\alpha_{vir} \sim 0.025$) are enough to cause a core to fragment and form more than one star, with the average number of stars growing as the level of turbulence is increased (Fontani et al. 2018). This trend is reflected in our simulations; as demonstrated in Table 1, the number of fragments increases from 1 to 4 to 9 as the turbulent Mach number grows from 0.18 to 0.35 to 0.49.

In most of our zoom-in simulations where the resolution is lower and the peak density is below 10^9 cm^{-3}, the total number of stars is ≤9, the total mass in stars exceeds by roughly 30 per cent the sink mass in the corresponding baseline simulation and the most massive star have sometimes a higher mass than 1/3 of the sink mass. We partially attribute this non-convergent result to the limited resolution. Indeed in core *A-hr*, that is our highest resolution zoom-in simulation, where the sink formation density reaches ∼10^{10} cm^{-3} (close to the density where the gas becomes adiabatic), 12 stars are formed, we reproduce very closely the stellar mass of the sink in the baseline simulation, our highest mass star is <1/3 of the baseline sink mass and we resolve low-mass stars down to 0.01 M$_\odot$.

It has been argued that the formation of low-mass stars from the fragmentation of massive cores contradicts the observations of a high binary fraction of low-mass stars (Goodwin et al. 2007). However, if the low-mass stars form in a hierarchical system as in our simulations, when they are ejected from the systems they can retain their binary companion. Indeed in core *A-hr* we observe binaries in disc stars and ejected binary systems, even though the limited resolution prevents us from resolving close binaries with separations <14 au. We will study stellar dynamics in more detail in future work.
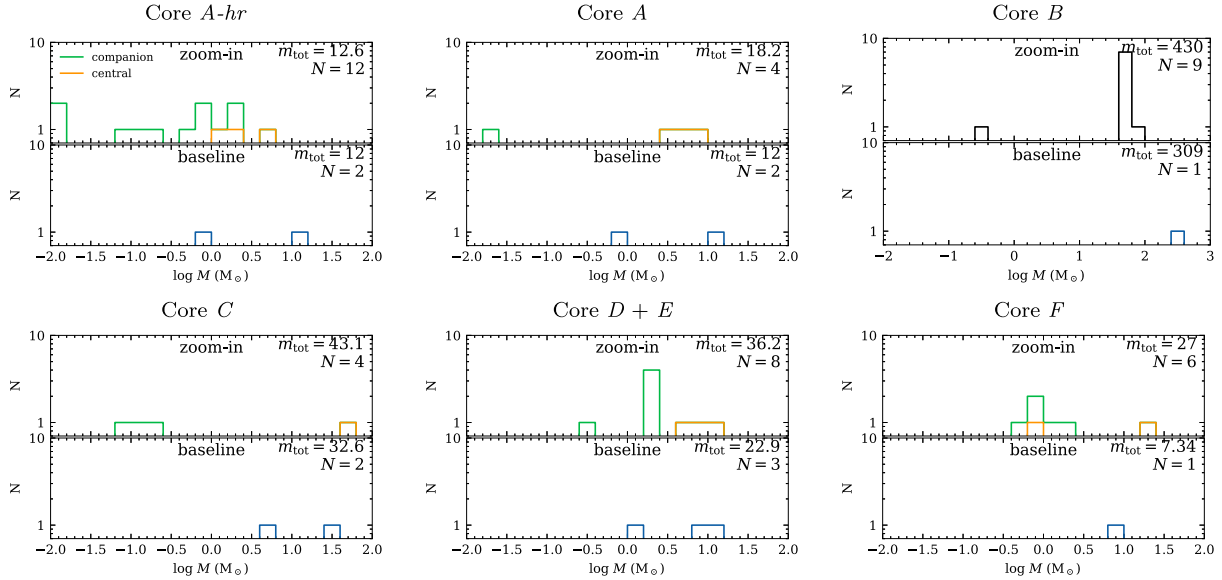
Figure 10. The mass distribution of the stars forming in each core in our 'zoom-in' simulations, labelled 'zoom-in', compared to the stars that form from the same core in the baseline run, labelled 'baseline'. The mass functions of the stars in the 'zoom-in' simulations are plotted in two colours to distinguish the central stars (orange) and companion stars (green), or in black when these two groups of stars are indistinguishable. In the case of cores *D* and *E*, because they are in close proximity to each other, their central stars, as well as their companion stars, are grouped together. Overall, the number of stars that form from the fragments of a core ranges from 1 to 12.

It remains to be seen if this type of fragmentation is realistic in small (< a few $M_\odot$) cores, given the observed levels of non-thermal motion therein which rules out any significant highly supersonic turbulence found in HM cores.

5 DISCUSSION

5.1 Formation of ultra-HM stars – a competitive accretion scenario

Recent advancement of radio/mm and optical/IR interferometers has enabled important progress in the field of discs around HM (early-B to late-O type) YSOs (see Davies et al. 2011; Mottram et al. 2011). The current unambiguous evidence for circumstellar discs around HM young stars is limited to objects with masses up to 30 $M_\odot$ (late-O type; Beltrán & de Wit 2016). Stars with these spectral types or brighter have strong UV emissions that can heat and disperse the gas. Typical disc radii of these sources are a few thousand au with rare exceptions of radii as small as 300–400 au. Most of the protostars in our simulations (Cores *A-hr*, *D*, *E*, *F*) fall in the range of HM stars, with Cores *B* and *C* forming stars that are over 40 $M_\odot$. The range of the radii of the simulated discs in this work (see Table 1) agrees well with the observations.

In the observations mentioned above, the circumstellar discs have typical gas masses ranging from 4 to a few × 10 $M_\odot$. In our simulations the masses of discs, defined as disc gas above a density threshold of ~10^5 cm^{-3}, ranges between 3 to 50 $M_\odot$, in agreement with the observed range. The disc mass remains relatively low (~40 $M_\odot$) even in the very massive core *B* where the central star cluster mass is above 600 $M_\odot$. This is due to the surface density being roughly constant at 8 g cm^{-2} up to a disc radius of ~6000 au, where the azimuthal velocity becomes comparable to the gas velocity dispersion, typically 1 to 3 km s^{-1}. Higher mass (up to 200 $M_\odot$) discs are only reported in a few cases where the angular resolution is not enough to properly separate the envelope from the disc (Beltrán et al. 2004).

At the lower bound of the HM range where there are enough nearby sources, observers are able to estimate the hydrostatic scale height of these structures from (sub)millimetre observations of the line width. The typical line width is found to be ~2 km s^{-1} and the estimated scale height is in most cases >30–40 per cent of the disc radius, indicating that the discs of embedded protostars are likely geometrically thick (e.g. Beltrán et al. 2006).

Both the velocity field probed via molecular lines at high angular resolution ($\leq 0.5''$) and the CO bandhead profile suggest that the rotation of the majority of the discs is consistent with Keplerian or quasi-Keplerian rotation (e.g. Wang, van der Tak & Hogerheijde 2012; Beltrán et al. 2014; Cesaroni et al. 2014). For some sources, observations reveal both sub-Keplerian (e.g. Cesaroni et al. 2005; Wang et al. 2012; Beltrán et al. 2014) and super-Keplerian (Beuther et al. 2008). Wang et al. (2012) argues that sub-Keplerian motions suggest a role for magnetic fields that could slow down the rotation below pure Keplerian by, i.e. magnetic braking. In our simulations, the discs are generally sub-Keplerian, with the non-Keplerianity parameter β_{kep} being in the range of −0.5 to −0.1. The low values of β_{kep} indicate a relatively large accretion rate from the large-scale envelope.

Another feature of protostellar discs of HM stars is the presence of asymmetries and inhomogeneities (e.g. Cesaroni et al. 2014). The authors claim that these asymmetries could be caused by the presence of spiral arms or infalling filaments accreting material on to the disc or by interacting with companions nearby. Discs that have been observed with an extremely high angular resolution where a clear disc structure could be resolved, appear to be slightly elongated and oriented perpendicular to molecular outflows (Wang et al. 2012; Beltrán et al. 2014). This structure is similar to the early phase of collapse of our simulated Case *B* core.

During the initial phase of collapse, our simulated core *B* has a spherical shape with a radius of ~0.5 parsec within a density threshold of 3000 cm^{-3}, enclosing a total mass of 131 $M_\odot$. The core has a density profile that is shallower than that of a Bonnor–Ebert sphere, with both magnetic and turbulent pressure in the envelope
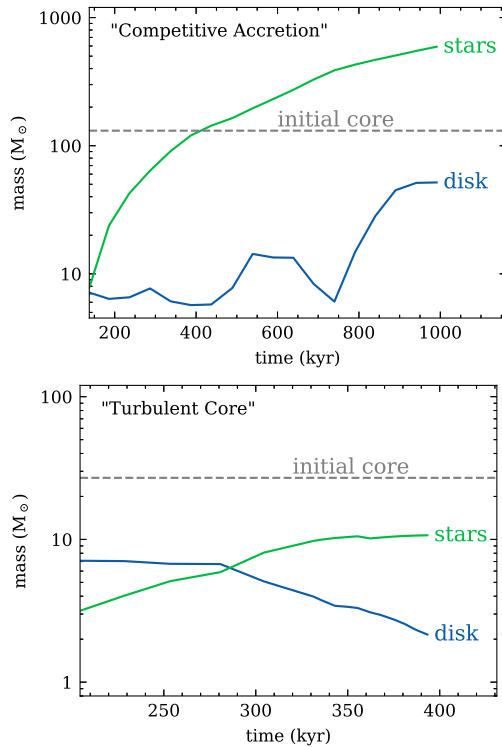
Figure 11. *Top*: The growth of Core *B* from a 130 M$_\odot$ core into a mini-cluster of stars with a total mass of ~600 M$_\odot$ and average mass of 70 M$_\odot$ via filamentary accretion from the background, demonstrating a CA scenario for ultra-HM star formation. *Bottom:* The collapse of 27 M$_\odot$ Core *A-hr* into a central binary of ~10 M$_\odot$ plus low-mass companions, demonstrating a 'TC' scenario for intemediate- to HM star formation. The colour curves show the evolution over time of the total mass in stars, labelled as 'stars', or the mass of the disc, labelled as 'disc'.

being 10 times stronger than thermal pressure (Fig. 5). However, the mass accreted in the central (proto)star cluster is >600 M$_\odot$ over a time-scale of about 0.9 Myr, more than four times the initial gas reservoir in the core (Fig. 11). This is due to the sustained high accretion rate (10^{-4}–10^{-3} M$_\odot$ yr^{-1}) over 0.9 Myr at a inflow velocity of 1 to 3 km s^{-1}. We, therefore, argue that the large masses (50–100 M$_\odot$) of the YSOs in core *B* can be described, at least partially, in the context of the CA scenario, in which the gas is collected over time from scales beyond the initial core radius. This agrees with Gong & Ostriker (2015) who, through a set of simulations of turbulent, unmagnetized GMCs, find that sink particles accrete at a nearly constant rate even after the initial mass reservoir is depleted. However, this kind of 'CA' is only seen in the most massive (>50 M$_\odot$) core in our simulations.

Observational evidence of circumstellar structures in the most massive protostars, i.e. early-O type, is very limited. Huge, dense, massive, rotating cores have been detected around early-O-type protostars in studies performed at moderate spatial resolutions. These objects are in all likelihood non-equilibrium structures surrounding clusters of young protostars and not merely individual massive stars (see Beltrán et al. 2011, and references therein). These structures are characterized by a much higher mass and larger size than the rotationally supported discs around lower mass protostars discussed above. Beltrán et al. (2005) referred to these massive structures as 'toroids' to make a distinction. The reported toroids have radii of a few × 1000 au to up to 10^4 au (e.g. Zapata et al. 2008). The hydrostatic scale height of these toroids, estimated by assuming

hydrostatic equilibrium, is > 50 per cent of the radius – these structures are extremely thick.

We find that the most massive stars in our star cluster formation simulations form as clusters inside large and dynamically stable toroids with significant mass infall. Our simulated Core *B* matches the properties of the toroids discussed above. The structure that enshrouds the central protostar cluster forms a toroid that is both large (4000–8000 au in radius) and thick (3000–8000 au in thickness) and is largely sub-Keplerian. The high infall rate, of the order of 10^{-3} M$_\odot$ yr^{-1}, could be high enough to quench the formation of an H II region or to slow down its expansion (Yorke 1986, see also Section 5.2). In the next section, we will show that core *B* produces a bipolar H II region and an outflow. However, in general, the question of whether or not the launching of outflows could be quenched initially by the massive envelope requires further studies that take into account jet-driven outflow and perhaps stellar winds.

5.2 UV radiation trapping

HM stars are often observed to be deeply embedded in dense gas and their H II regions in the gas above a density of ~10^4 cm^{-3} can remain trapped forming ultracompact H II regions (Churchwell 2002; Jaura et al. 2022). In our simulated pre-stellar cores, we notice two main distinct scenarios: A) when a single massive star is deeply embedded in a thick disc, where the density reaches ~10^8 cm^{-3}, the H II regions remain trapped at least during the first 0.5 Myr while the disc is still relatively massive. B) Often massive stars orbit a common centre of mass in binary or multiple star systems: in these cases the stellar orbit may displace the massive star from the densest regions in the disc or in a filament, allowing the H II regions to break out the dense disc or filament. Case A) can be observed in the left-hand panels of Fig. 12), showing core *D*, where a single massive star forms from the collapse of the small core. The UV radiation of the protostar is trapped inside the dense neutral gas The H II region remains trapped for a few hundred kiloyears. Note that the consumption rate of ionizing photons, emitted uniformly within the sink particles, is equal to the recombination rate in the ionized gas calculated in each cell, even inside the sink particles. However, here we do not adopt any sub-sink recipe to account for the radiation transfer inside the poorly resolved density structure within the sinks, as done in other studies (Jaura et al. 2022; Park, Ricotti & Sugimura 2023). In Core *A-hr*, however, multiple stars form at or migrate into the disc centre (see right-hand panels of Fig. 12). The dynamics of the few-body star system displaces the stars by about the virial radius of the star system, which is tens of au, close to or higher than the disc thickness. In this case, radiation can escape when one of the massive stars approaches the edges of the disc. Once a channel of lower density ionized gas is created a long-lasting bipolar H II region and outflow are created.

Finally, Fig. 13 shows another interesting mechanism that allows UV ionizing radiation to break out of a dense filament. The figure shows the density (top panels) and the temperature (bottom panels) in a set of snapshots showing a disc embedded in a filament in which a multiple system, including a massive star, forms. The stars are shown as circles colour coded according to their masses from white (1 M$_\odot$) to dark green (10 M$_\odot$). From the time sequence, it is clear that H II regions are created intermittently on either side of the filament when the massive star in its orbit is further from the densest part of the filament, allowing the H II region to break out of the filament. This is more evident in the animation that we make available in the electronic version of this paper.
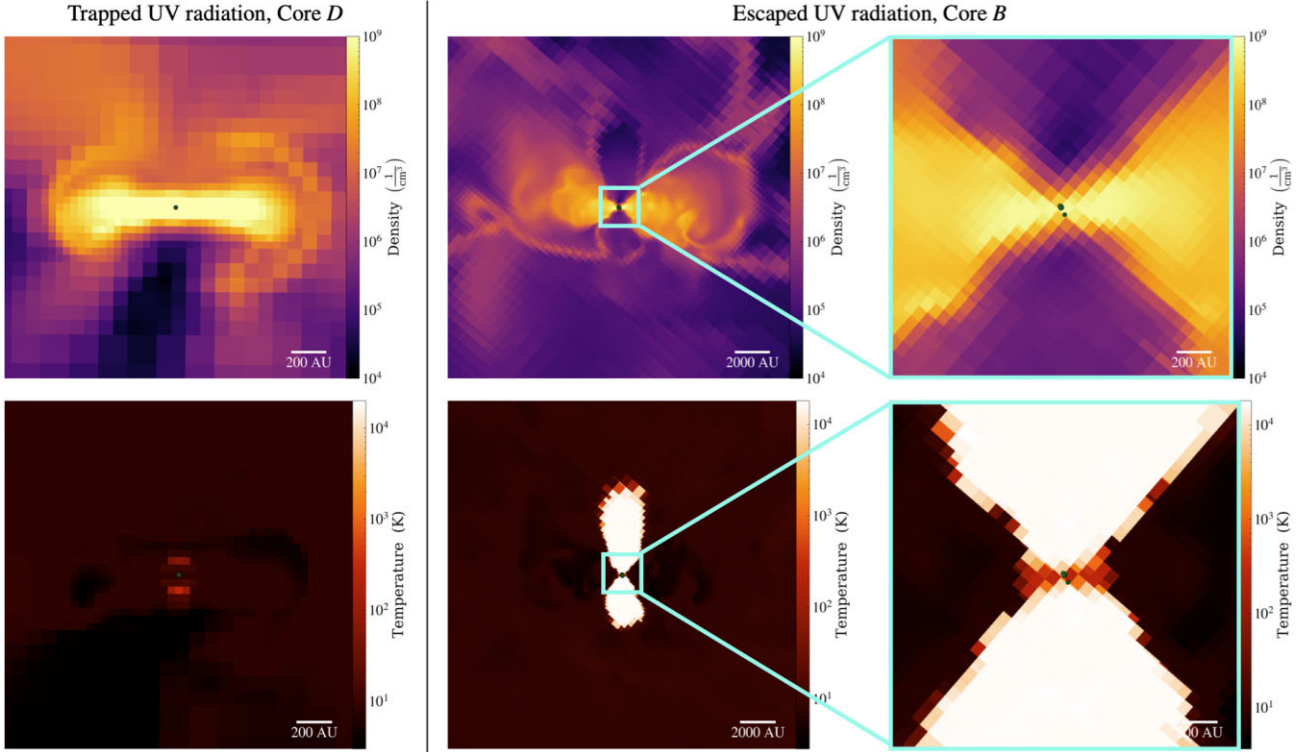
Figure 12. The trapping (left) and escaping (right) of H II regions. *Left*: Density (top) and temperature (bottom) slices of core *D* showing the UV radiation from an ∼10 M$_\odot$ star is trapped inside an ultracompact region at the centre of a disc. *Right*: Similar to *Left* but for the Core *B* showing the escaping of an ultracompact H II region. The dynamical motions of the multistar system create a channel for radiation to escape.
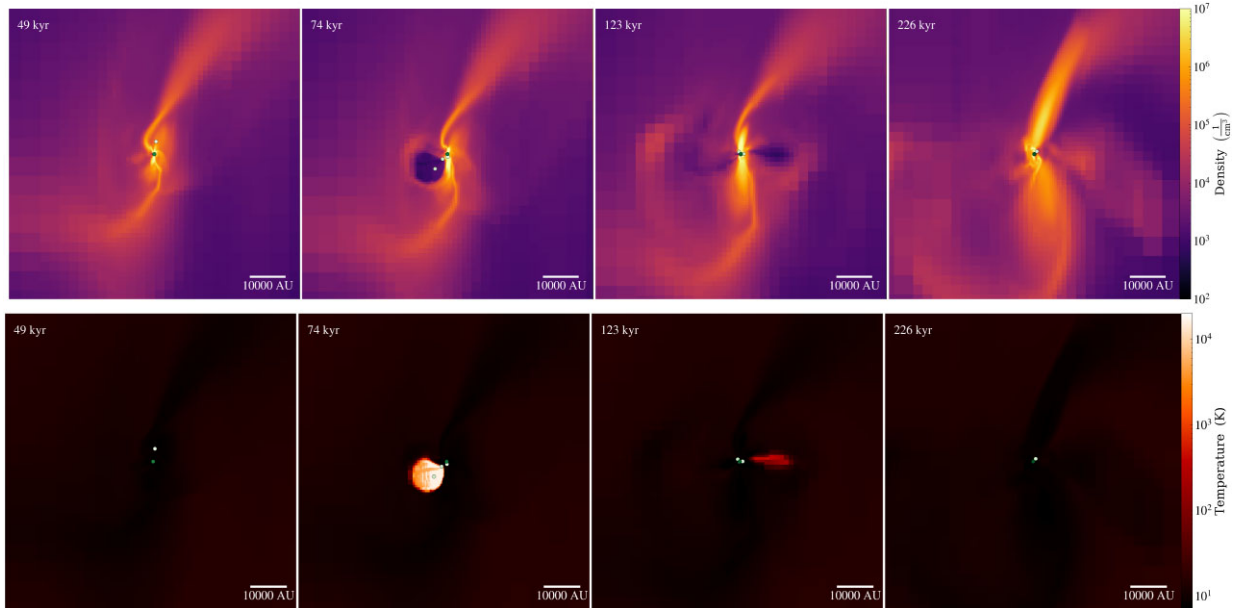

Figure 13. The escaping of UV radiation from a dense filament due to dynamical motion. From left to right, it shows a time sequence of the density (top) and temperature (bottom) slices. The dancing of the stars creates a channel for UV photons to escape from the dense region and create a channel of photoionization when a massive star dynamically reaches the edge of the disc.

5.3 Influence of metallicity on disc stability

Our simulations are conducted at solar metallicity and the cooling from hydrogen, helium, carbon, oxygen, and dust grains. Lower metallicity could make a big difference in how the disc fragments.

Recent study (Matsukoba et al. 2022) of the metallicity dependence of protostellar-disc fragmentation has shown that fragmentation of spiral arms is more common in lower metallicities where dust cooling is effective. At high metallicity, the disc is stabilized by stellar irradiation. We find that despite being cold (close to 10 K) due to the

lack of effective heating from the stars, the discs are stable and do not undergo fragmentation, as discussed in Section 4.1.

6 SUMMARY

We have simulated the formation and collapse of pre-stellar cores in a set of grid-based radiation-MHD simulations, resolving from GMC scales, tens-of-parsec in size, down to disc scales, with resolutions up to 7 au in our highest resolution simulation.

We studied a set of six massive (~ 10 M$_\odot$) or very massive (~ 100 M$_\odot$) cores in two GMCs, following their collapse, fragmentation, and the formation of (proto)stars embedded in circumstellar discs with sizes ranging from 200 to 6000 au. The properties of the simulated cores, and the (proto)stars and discs that form therein are listed in Table 1.

The following is a list of the main results:

(i) The discs are generally large ($R = 200$–6000 au), thick (aspect ratio $H/R = 0.2 - 1.3$), and massive with masses spanning from a few to 40 M$_\odot$ (Table 1 and Fig. 2). These discs or toroids sit in the range of observed disc properties around HM YSOs.

(ii) Each core undergoes fragmentation in the early collapsing phase with geometries that can be separated into two main distinct modes: 'quasi-spherical' collapse and 'filamentary' collapse (see Fig. 3). However, in both modes of collapse, the fragments eventually become embedded in a quasi-steady accretion disc or toroid.

(iii) We observe the formation of multiple massive stars at the centre of the disc, but also lower mass stars apparently forming in outer parts of the disc. However, the disc is on average Toomre-stable. We find that 'disc stars' form from pre-existing self-gravitating fragments created before the formation of the gravitationally stable discs and are accreted into the disc as mentioned in the point above (see Figs 3 and 9). We, therefore, conclude that in order to realistically simulate the formation and evolution of massive stars and their circumstellar discs it is crucial to capture the environment and initial conditions of the protostellar core. Idealized initial conditions starting from smooth disc structures, often used to model circumstellar discs around solar-mass stars, will likely not capture the full picture of fragmentation of the disc for the HM case.

(iv) Large and massive discs around HM stars are supported by both magnetic and turbulent pressure. This is in contrast to the case of discs around lower mass stars, supported instead by thermal pressure. Regardless of the core mass/size, the magnetic pressure dominates in the envelope as well as the outer disc at radii $\gtrsim$200–1000 au, while turbulent pressure dominates in the inner disc at <200–1000 au (see Fig. 8). The turbulent velocity of the disc is close to the virial velocity of the core, including the central protostars (~ 1 km s^{-1}), which suggests that the source of the turbulence is the non-axisymmetric gravitational collapse of the gas.

(v) The final number of (proto)stars that form in a core is between 1 and 12 (Fig. 10). Most of the accreted mass is distributed among 1 to 3 stars of similar mass (up to a mini cluster of 8 stars for our most massive core) that form near the centre of the disc/toroid. The disc stars account for a small or negligible fraction of the mass of stars.

(vi) In our highest resolution simulation ($\Delta x_{\min} = 7$ au) where the sink formation density is above 10^{10} cm^{-3}, close to the density where the gas becomes adiabatic, the total mass in stars (12.6 M$_\odot$) is approximately equal to the mass of the sink particle in the baseline run, which is believed to represent a pre-stellar core. This suggests a nearly 100 per cent SFE in HM cores.

(vii) In the most massive core we simulated, the core evolves from a spherical shape with a radius of 0.5 parsec and a mass of 131 M$_\odot$

into a (proto)star cluster that is over 600 M$_\odot$ enshrouded by a massive toroid over a time-scale of about 0.9 Myr (Fig. 11). We explain the large masses in these ultra-HM (proto)stars in the context of the CA scenario, in which gas is continuously supplied from larger scales beyond the mass reservoir of the core.

(viii) O/B stars that form as a single star typically produce an ultracompact H II region that remains trapped in the dense and thick circumstellar disc for an extended period of time ($\sim$500 kyr). However, when HM stars form as wide binaries or in multiple systems, the dynamic motion of the system displaces the stars periodically from the densest parts in the disc plane or filament where the density is lower allowing UV radiation to escape and creating a long-lasting or periodic bipolar H II regions (see Figs 12 and 13).

In a companion paper, we will further study the properties and growth of the magnetic field in magnetically critical and subcritical cores, where we will also address the origin of the density-*B* relationship and the magnetic breaking problem.

DATA AVAILABILITY

The data underlying this article were accessed from the University of Maryland supercomputing resources (http://hpcc.umd.edu). The derived data generated in this research will be shared on reasonable request to the corresponding author. The software used to do the analysis in this paper is RAMTOOLS, a toolkit to postprocess RAMSES simulations that are based on the YT toolkit (https://yt-project.org/doc/index.html) and are available to download from https://chongchonghe.github.io/ramtools-pages/.

REFERENCES

Agertz O. et al., 2007, MNRAS, 380, 963
Alves J., Lombardi M., Lada C. J., 2007, A&A, 462, L17
André Oliva G., Kuiper R., 2020, A&A, 644, A41
Andrews S. M., Wilner D. J., Hughes A. M., Qi C., Dullemond C. P., 2009, ApJ, 700, 1502
Bate M. R., 2019, MNRAS, 484, 2341
Bate M. R., Burkert A., 1997, MNRAS, 288, 1060
Bate M. R., Bonnell I. A., Bromm V., 2003, MNRAS, 339, 577
Belloche A., 2013, in Hennebelle P., Charbonnel C.eds, EAS Publ. Ser. Vol. 62, Role and Mechanisms of Angular Momentum Transport During the Formation and Early Evolution of Stars, Evry Schatzman School 2012. Cambridge Univ. Press, Cambridge, p. 25
Beltrán M. T., de Wit W. J., 2016, A&AR, 24, 6
Beltrán M. T., Cesaroni R., Neri R., Codella C., Furuya R. S., Testi L., Olmi L., 2004, ApJ, 601, L187
Beltrán M. T., Cesaroni R., Neri R., Codella C., Furuya R. S., Testi L., Olmi L., 2005, A&A, 435, 901
Beltrán M. T., Cesaroni R., Codella C., Testi L., Furuya R. S., Olmi L., 2006, Nature, 443, 427
Beltrán M. T., Cesaroni R., Neri R., Codella C., 2011, A&A, 525, A151
Beltrán M. T. et al., 2014, A&A, 571, A52
Beuther H., Walsh A. J., Thorwirth S., Zhang Q., Hunter T. R., Megeath S. T., Menten K. M., 2008, A&A, 481, 169

Bleuler A., Teyssier R., 2014, MNRAS, 445, 4015

Bonnell I. A., Bate M. R., Clarke C. J., Pringle J. E., 2001, MNRAS, 323, 785

Casassus S. et al., 2015, ApJ, 811, 92

Caselli P., Benson P. J., Myers P. C., Tafalla M., 2002, ApJ, 572, 238

Cesaroni R., Neri R., Olmi L., Testi L., Walmsley C. M., Hofner P., 2005, A&A, 434, 1039

Cesaroni R., Galli D., Lodato G., Walmsley C. M., Zhang Q., 2007, in Reipurth B., Jewitt D., Keil K.eds, Protostars and Planets V. Univ. Arizona Press, Tucson, p. 197

Cesaroni R., Galli D., Neri R., Walmsley C. M., 2014, A&A, 566, A73

Cheng Y. et al., 2022, ApJ, 933, 178

Chon S., Hosokawa T., 2019, MNRAS, 488, 2658

Churchwell E., 2002, ARA&A, 40, 27

Davies B., Hoare M. G., Lumsden S. L., Hosokawa T., Oudmaijer R. D., Urquhart J. S., Mottram J. C., Stead J., 2011, MNRAS, 416, 972

de Wit W. J., Hoare M. G., Oudmaijer R. D., Nürnberger D. E. A., Wheelwright H. E., Lumsden S. L., 2011, A&A, 526, L5

Elmegreen B. G., 2000, ApJ, 530, 277

Elmegreen B. G., Scalo J., 2004, ARA&A, 42, 211

Espaillat C., Furlan E., D'Alessio P., Sargent B., Nagel E., Calvet N., Watson D. M., Muzerolle J., 2011, ApJ, 728, 49

Fontani F. et al., 2016, A&A, 593, L14

Fontani F., Commerçon B., Giannetti A., Beltrán M. T., Sánchez-Monge Á., Testi L., Brand J., Tan J. C., 2018, A&A, 615, A94

Fromang S., Hennebelle P., Teyssier R., 2006, A&A, 457, 371

Fukushima H., Yajima H., Sugimura K., Hosokawa T., Omukai K., Matsumoto T., 2020, MNRAS, 497, 3830

Fuller G. A., Williams S. J., Sridharan T. K., 2005, A&A, 442, 949

Galli D., Shu F. H., 1993, ApJ, 417, 243

Gaudel M. et al., 2020, A&A, 637, A92

Geen S., Soler J. D., Hennebelle P., 2017, MNRAS, 471, 4844

Ginsburg A., Bally J., Goddi C., Plambeck R., Wright M., 2018, ApJ, 860, 119

Gong M., Ostriker E. C., 2015, ApJ, 806, 31

Goodman A. A., Benson P. J., Fuller G. A., Myers P. C., 1993, ApJ, 406, 528

Goodwin S. P., Whitworth A. P., Ward-Thompson D., 2004a, A&A, 414, 633

Goodwin S. P., Whitworth A. P., Ward-Thompson D., 2004b, A&A, 423, 169

Goodwin S. P., Kroupa P., Goodman A., Burkert A., 2007, in Reipurth B., Jewitt D., Keil K.eds, Protostars and Planets V. Univ. Arizona Press, Tucson, p. 133

Grudić M. Y., Guszejnov D., Hopkins P. F., Offner S. S. R., Faucher-Giguère C.-A., 2021, MNRAS, 506, 2199

Guzmán A. E., Sanhueza P., Zapata L., Garay G., Rodríguez L. F., 2020, ApJ, 904, 77

Hansen C. E., Klein R. I., McKee C. F., Fisher R. T., 2012, ApJ, 747, 22

He C.-C., Ricotti M., Geen S., 2019, MNRAS, 489, 1880

He C.-C., Ricotti M., Geen S., 2020, MNRAS, 492, 4858

Hennebelle P., Fromang S., 2008, A&A, 477, 9

Ilee J. D., Cyganowski C. J., Brogan C. L., Hunter T. R., Forgan D. H., Haworth T. J., Clarke C. J., Harries T. J., 2018, ApJ, 869, L24

Jaura O., Glover S. C. O., Wollenberg K. M. J., Klessen R. S., Geen S., Haemmerlé L., 2022, MNRAS, 512, 116

Johnston K. G. et al., 2015, ApJ, 813, L19

Johnston K. G. et al., 2020, A&A, 634, L11

Jones M. O., Bate M. R., 2018, MNRAS, 478, 2650

Joos M., Hennebelle P., Ciardi A., 2012, A&A, 543, A128

Kim J.-G., Kim W.-T., Ostriker E. C., 2018, ApJ, 859, 68

Kim J.-G., Ostriker E. C., Filippova N., 2021, ApJ, 911, 128

Kratter K., Lodato G., 2016, ARA&A, 54, 271

Kraus S. et al., 2010, Nature, 466, 339

Kroupa P., 2002, Science, 295, 82

Krumholz M. R., Matzner C. D., 2009, ApJ, 703, 1352

Krumholz M. R., Klein R. I., McKee C. F., 2007, AJ, 656, 959

Krumholz M. R., Klein R. I., McKee C. F., Offner S. S. R., Cunningham A. J., 2009, Science, 323, 754

Krumholz M. R., Klein R. I., McKee C. F., 2011, ApJ, 740, 74

Kuffmeier M., Haugbølle T., Nordlund Å., 2017, ApJ, 846, 7

Kuffmeier M., Calcutt H., Kristensen L. E., 2019, A&A, 628, A112

Kuiper R., Klahr H., Beuther H., Henning T., 2010, ApJ, 722, 1556

Kuiper R., Turner N. J., Yorke H. W., 2016, ApJ, 832, 40

Law C.-Y. et al., 2022, ApJ, 939, 120

Lee Y.-N., Hennebelle P., 2018, A&A, 611, A88

Machida M. N., Omukai K., Matsumoto T., Inutsuka S.-i., 2008, ApJ, 677, 813

Marino S., Perez S., Casassus S., 2015, ApJ, 798, L44

Masunaga H., Inutsuka S.-i., 2000, ApJ, 531, 350

Masunaga H., Miyama S. M., Inutsuka S.-i., 1998, ApJ, 495, 346

Matsukoba R., Tanaka K. E. I., Omukai K., Vorobyov E. I., Hosokawa T., 2022, MNRAS, 515, 5506

McKee C. F., Tan J. C., 2003, ApJ, 585, 850

Mottram J. C. et al., 2011, ApJ, 730, L33

Muzerolle J. et al., 2009, ApJ, 704, L15

Offner S. S. R., Chaban J., 2017, ApJ, 847, 104

Olguin F. A., Sanhueza P., Ginsburg A., Chen H.-R. V., Zhang Q., Li S., Lu X., Sakai T., 2022, ApJ, 929, 68

Padoan P., Pan L., Juvela M., Haugbølle T., Nordlund Å., 2020, ApJ, 900, 82

Park J., Ricotti M., Sugimura K., 2021a, MNRAS, 508, 6176

Park J., Ricotti M., Sugimura K., 2021b, MNRAS, 508, 6193

Park J., Ricotti M., Sugimura K., 2023, MNRAS, 521, 5334

Patel N. A. et al., 2005, Nature, 437, 109

Rosdahl J., Blaizot J., Aubert D., Stranex T., Teyssier R., 2013, MNRAS, 436, 2188

Rosen A. L., Krumholz M. R., McKee C. F., Klein R. I., 2016, MNRAS, 463, 2553

Rosenfeld K. A. et al., 2012, ApJ, 757, 129

Sánchez-Monge Á., Palau A., Estalella R., Kurtz S., Zhang Q., Di Francesco J., Shepherd D., 2010, ApJ, 721, L107

Stacy A., Greif T. H., Bromm V., 2010, MNRAS, 403, 45

Sugimura K., Ricotti M., 2020, MNRAS, 495, 2966

Takahashi S., Saigo K., Ho P. T. P., Tomida K., 2012, ApJ, 752, 10

Tan J. C., Beltrán M. T., Caselli P., Fontani F., Fuente A., Krumholz M. R., McKee C. F., Stolte A., 2014, in Beuther H., Klessen R. S., Dullemond C. P., Henning T.eds, Protostars and Planets VI. Univ. Arizona Press, Tucson, p. 149

Teyssier R., 2002, A&A, 385, 337

Vacca W. D., Garmany C. D., Shull J. M., 1996, ApJ, 460, 914

van Kempen T. A., Longmore S. N., Johnstone D., Pillai T., Fuente A., 2012, ApJ, 751, 137

Verliat A., Hennebelle P., Maury A. J., Gaudel M., 2020, A&A, 635, A130

van der Tak F. F. S., Shipman R. F., Jacq T., Herpin F., Braine J., Wyrowski F., 2019, A&A, 625, A103

Wang K. S., van der Tak F. F. S., Hogerheijde M. R., 2012, A&A, 543, A22

Williams G. M. et al., 2022, MNRAS, 509, 748

Yorke H. W., 1986, ARA&A, 24, 49

Zapata L. A., Ho P. T. P., Rodríguez L. F., Schilke P., Kurtz S., 2007, A&A, 471, L59

Zapata L. A., Palau A., Ho P. T. P., Schilke P., Garrod R. T., Rodríguez L. F., Menten K., 2008, A&A, 479, L25

SUPPORTING INFORMATION

Supplementary data are available at *MNRAS* online.

zoom-HII-escape.mp4

Please note: Oxford University Press is not responsible for the content or functionality of any supporting materials supplied by the authors. Any queries (other than missing material) should be directed to the corresponding author for the article.

This paper has been typeset from a TEX/LATEX file prepared by the author.